A 3-D Radiative Transfer Analysis of AGB Winds

Seán Vivian Clarke
13437318

Supervisor:

Dr. M.P. Redman

OLLSCOIL NA GAILLIMHE
UNIVERSITY OF GALWAY

SUBMITTED IN FULFILMENT OF THE REQUIREMENTS FOR THE DEGREE OF
Master of Science

Centre for Astronomy,
School of Natural Sciences,
University of Galway

AUGUST 2023

ABSTRACT

The chemical enrichment of the interstellar medium is driven by stars of low to intermediate masses shedding their external layers through powerful stellar winds. Eventually, after many years in this phase, the core of the star ionises these expelled layers and becomes a planetary nebula, where the shape and morpology of the surrounding gas was imprinted during the previous mass loss phase of its life.

In this project, two aims are established. The first, to test two 3-D radiative transfer codes, MOLLIE and LIME, which were written for cold molecular clouds in their ability to model the conditions present in stellar winds of these asymptotic giant branch stars. The second is then using a code to model observational data of such a star.

Two models were constructed for this work in accordance with the two aims established. The first model is a representation of the conditions present within the circumstellar envelope of an asymptotic giant branch star while the second is a model of the star IK Tauri, using literature and the code itself to constrain the parameters for accurately modelling the outflow. Both models use carbon monoxide as the rotational molecule due to its proliferation throughout stars and that it closely follows hydrogen lines while also being much visible than hydrogen itself.

From the analysis of the test model, we determined MOLLIE unfit for the purpose of this work, so further modelling was carried out by LIME alone. With LIME we obtained accurate fits to the IK Tauri data for each rotational line, isotopolgue, and resolution studied. This verifies that the relatively simple model could produce line profiles supported by observational data while being less complex in comparison to 1-D radiative transfer models for similar results.

AUTHOR'S DECLARATION

I declare that the work in this thesis is based on research carried out at the Centre for Astronomy, School of Physics, National University of Ireland, Galway. No part of this thesis has been submitted elsewhere for any other degree or qualification and it is all my own work unless referenced to the contrary in the text.

SIGNED: 

DATE: 29/08/23

ACKNOWLEDGEMENTS

I would first like to express my deepest gratitude to my supervisor, Dr. Matt Redman, who's continued support and guidance from the beginning right up to now at the end was always welcome.

I would also like to give sincere thanks to Dr. Nevenoe Guegan, who despite being busy with his own modelling would always make time to help improve my understanding of MOLLIE which then made working with LIME a smoother process as well.

To my parents, sisters, and brother, without them I'd probably not have gotten this far. My friends, scattered as they are, for keeping in touch throughout this project and especially to Conor, I have missed our weekly(ish) Ward's.

And to Niamh, for her near limitless patience.

TABLE OF CONTENTS

CHAPTER 1

INTRODUCTION TO SUBMILLIMETRE STUDIES OF EVOLVED STAR SYSTEMS

The space between stars, molecular clouds, planetary nebulae, black holes, and every astronomical object within this galaxy, the interstellar medium (ISM), is known to be an almost perfect vaccuum. But aside from these objects and others within it, what prevents space from being just that, an empty expanse devoid of all matter? A first thought might be because of supernovae, the cataclysmic explosions of massive supergiant stars which can seed the dust clouds of stellar nurseries with the heavy elements that can only be formed by the heat and pressure of a supergiant's core. However it is the smaller, but by no means small, Asymptotic Giant Branch stars which dominate the production and distribution of elements in the galaxy (Schröder et al., 1999).

AGB stars enrich the ISM by means of stellar winds carrying dust into the galaxy at large. Over time, and with many such stars contributing, the galaxy is slowly permeated with a variety of elements. This chemical evolution is then supplemented by the aforementioned supernova explosions bringing the heavy elements unique to them. Between these sources of enriched dust and elements they influence the composition of stars and planets formed from them which will then do the same in turn once they reach the end of their life cycle. See Figure 1.1 for an illustration on the relative contribution these processes have on the chemical evolution of the ISM.

In comparison with the explosive end of a supergiant, AGB stars have slower ends, with the

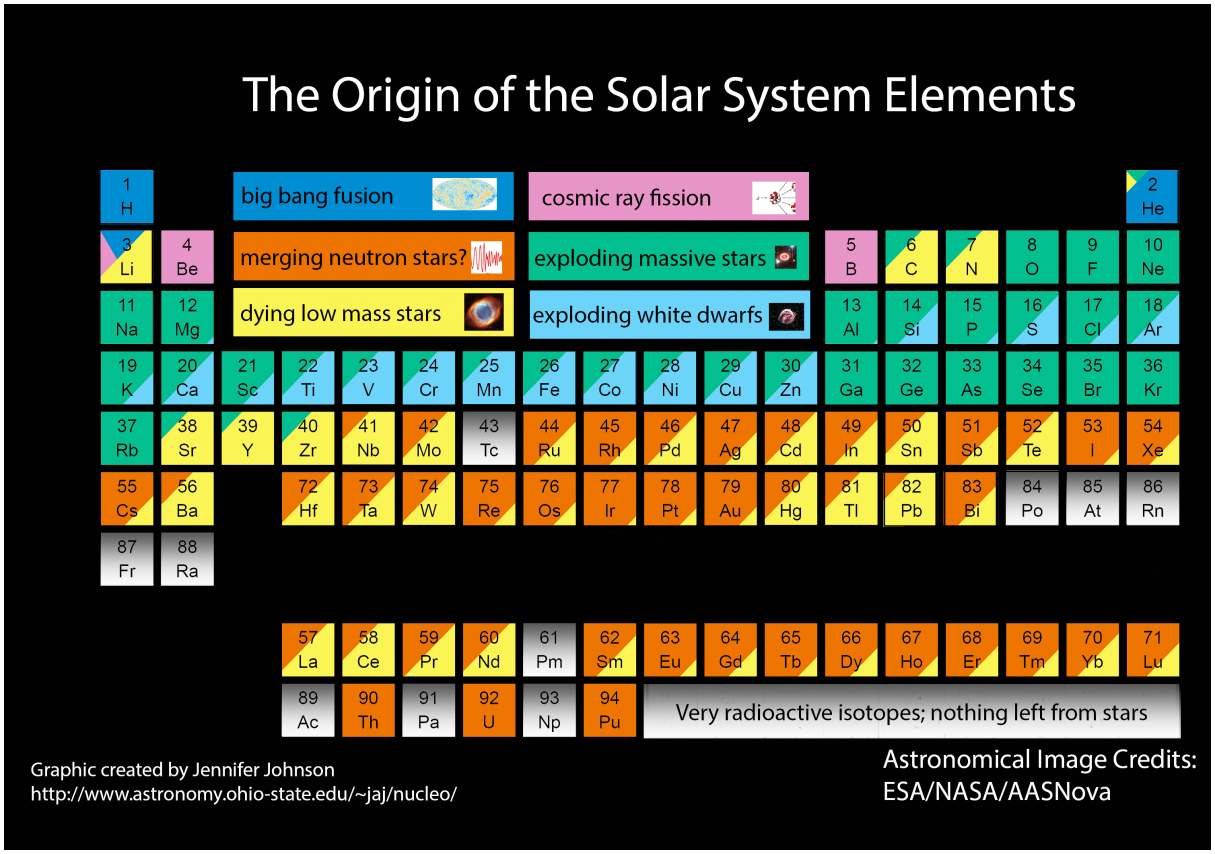

Figure 1.1: *This periodic table of the elements shows the contribution of 4 stellar processes (as well as Big Bang nucleosynthesis and cosmic ray spallation) to the abundance of elements throughout the galaxy. The production of carbon and nitrogen is dominated by dying stars from the AGB phase and we can also see that heavy metals come exclusively from supernova explosions. Image credit: Jennifer Johnson.*

mass loss from ejecting elements over the course of their lifetime resulting in their surrounding envelope being ejected as a gaseous cloud about the still burning core. What this has resulted in is a planetary nebula surrounding a white dwarf. These nebulae have varied and striking appearances, illuminated as they are by the white dwarf star. Through the study of AGB stars as they supply the ISM with material we look to gain a better understanding of what influences the morphology of these luminous gas clouds.

1.1 Evolution of an Asymptotic Giant Branch Star

Late in the life of a low to intermediate mass star (between 0.8 and 8 $M_{\odot}$), they will leave the main sequence and begin to evolve onto the asymptotic giant branch (AGB) phase (Danilovich et al., 2020). To reach this phase, the star will first go through the red giant

branch phase wherein the hydrogen (H) burning moves from the core to a thin shell which surrounds the now inert helium (He) core. At this stage the star's core will begin to contract as the envelope expands. At the end of this phase the core will have contracted enough to reach temperatures (10-100 million Kelvin) capable of fusing He (Höfner & Olofsson, 2018) and will begin to move horizontally along the Hertzsprung-Russell diagram as its temperature increases, see Figure 1.2.

The star continues to evolve slowly along the horizontal phase until all the He in the core is depleted. The core is now comprised of carbon/oxygen surrounded by a new He burning shell which in turn is enveloped by the H burning shell. Fusion then ceases in the core of the star, which contracts as the envelope expands and it now ascends the AGB, with mass loss driven by the slow stellar wind outflow.

At this point most of the energy output of the star comes from the H burning shell around the core (Wood & Zarro, 1981). The He shell now undergoes a cyclic process of He shell flashes or thermal pulses, with the luminosity and radiation pressure now so high and the envelope so large that the outermost layers are only weakly bound by gravity. These layers are particularly vulnerable during the periods of increased activity that sees a much higher rate of mass loss, which now over time leads to the loss of a substantial fraction of the star's mass, with the velocity of the stellar winds from the nucleus of the star being one or two magnitudes greater than the winds from earlier in its life (Osterbrock, 1964).

The cycle repeats until the circumstellar envelope (CSE) is blown off entirely and the carbon/oxygen core is revealed as a low mass (average being between 0.5 and 0.7 $M_{\odot}$ (Kepler et al. 2007)), but incredibly dense white dwarf star in the centre of a planetary nebula (PN) formed by the wind from the core colliding with and overtaking the slower red giant wind (Kwok et al., 1978). The PN is illuminated by the revealed core via UV photons which ionise the gas (Kwok, 2018).

These stars are of interest as planetary nebulae have varied morphologies, see Table 1.1, and it is in the AGB phase that the shape of the PN is imprinted. Possible candidates for effecting the shape of a nebula are binary companions, both stellar and substellar (Soker, 2004). Resolving these compact and often dust shrouded objects has become much more feasible with advances in radio and submillimetre astronomy such as with the Atacama Large Millimeter Array (ALMA) in Chile and the Submillimetre Array (SMA) in Hawaii.

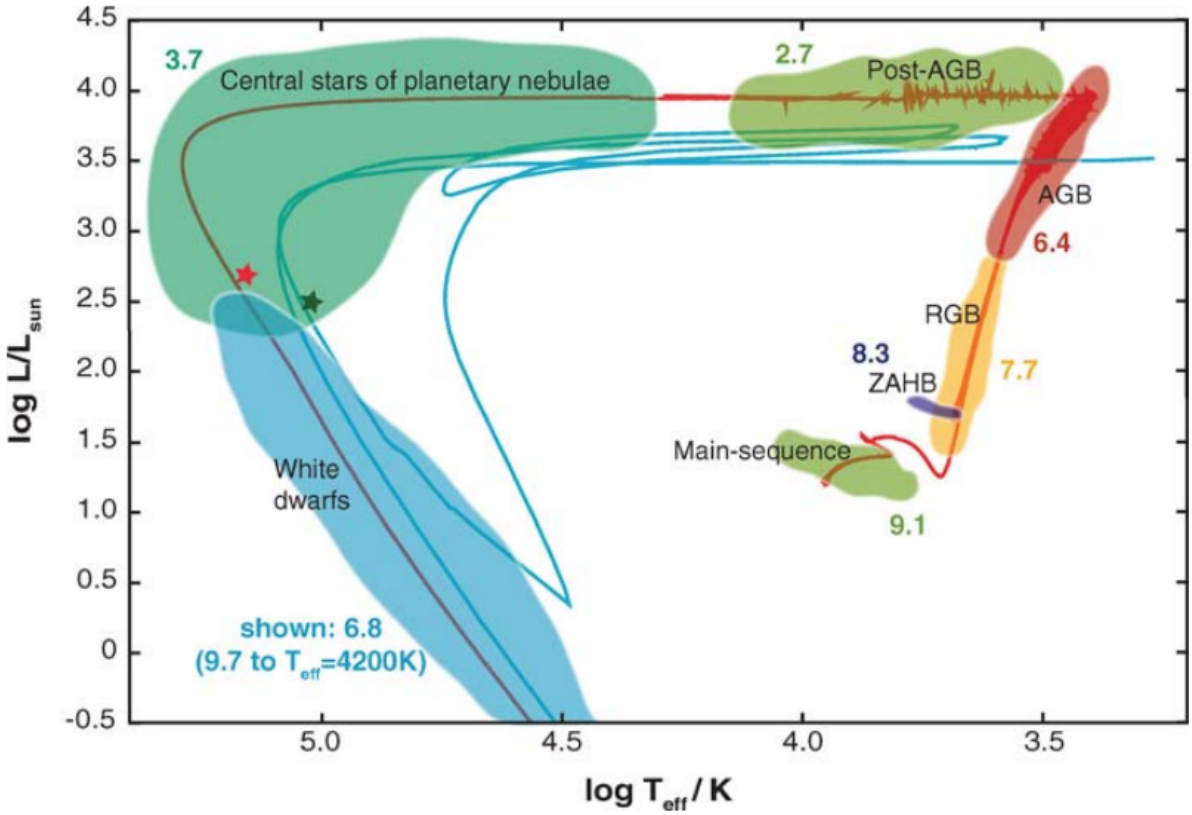

Figure 1.2: *Evolutionary path of a 2 $M_{\odot}$ star from the Main-sequence though the AGB phase to completion with the white dwarf phase. Horizontal branch labelled here as Zero Age Horizontal Branch. The colour-coded number labels give the log of the approximate duration of each phase in years for such a star. For the white dwarf phase, if the diagram was continued to track the star for $10^{9.7}$ years, it would cool to T_{eff} = 4200K (Herwig, 2005).*

Class	Total number	Per cent fraction	$\langle\|b\|\rangle$	σ	$n > 10$ arcsec
E: elliptical	492	54.4	3.50	2.39	432
R: round	175	19.3	4.05	2.51	146
B: bipolar	113	12.5	2.51	1.84	109
I: irregular	39	4.3	3.23	2.02	39
A: asymmetric	36	4.0	3.44	2.80	36
S: star-like	50	5.5	3.03	2.31	0

Table 1.1: *Table of morphologies for 903 PNe catalogued by MASH (Parker et al., 2006).*

1.2 Submillimetre Astronomy

Submillimetre astronomy is not suited to resolving the visible surfaces of stars. However, the CSE which surrounds an AGB provides the necessary conditions of temperature and density to facilitate the formation of excited molecules that emit electromagnetic wavelengths despite the source remaining shrouded (Burke & Graham-Smith, 2009). It is the CSE itself and surrounding dust clouds that obscure much of the structure within for traditional (visible wavelengths) observations, so it is from the emissions of the CSE that we look to for information on the star's physical conditions. By observing the submillimetre emissions from these sources, details in the structure of the envelopes and outflows can be resolved with improved clarity (Hirano et al., 2004).

From the molecular emissions and dust continuum emission lines we obtain information such as the structure or composition of the medium in terms of the atoms and molecules that give the emission lines (Bot et al., 2007), as well as density and temperature from the difference in energy levels of the transitions. Then through spectroscopic analysis of the line, the abundance of species in the medium can be gathered as well as the velocity of the system from the observed doppler shift of the wavelength's transition. The turbulence can then be estimated by the broadening of the spectral line, both through turbulence caused by shocks or thermal doppler broadening from hotter internal gases moving faster than the cooler external ones.

For choosing a target source for this work, the M-type Mira variable IK Tauri was selected. As an M-type giant, it is rare among giants at about 4% of total giant stars (giant stars dominated by K-type spectral class) whereas M-types in general make up 76% of main sequence stars due to the number of faint red dwarfs in the class which are mostly invisible to the naked eye (LeDrew, 2001).

At any rate, the naked eye is not a great tool for studying distant stars whether they be giants or dwarfs. With the ALMA interferometer however, the emissions, such as from the twelve AGB stars pictured in Figure 1.3 or with the Hubble Space Telescope in Figure 1.4, they can be studied with comparative ease. Figure 1.3 displays a variety of wind outflows and their doppler shift from the local standard of rest, and in 1.4 we can see the individual layers of the CSE as they had been blown off the star through mass loss. We can see some morphologies in line with those in Table 1.1, with round, elliptical, as well as some completely irregular

outflows.

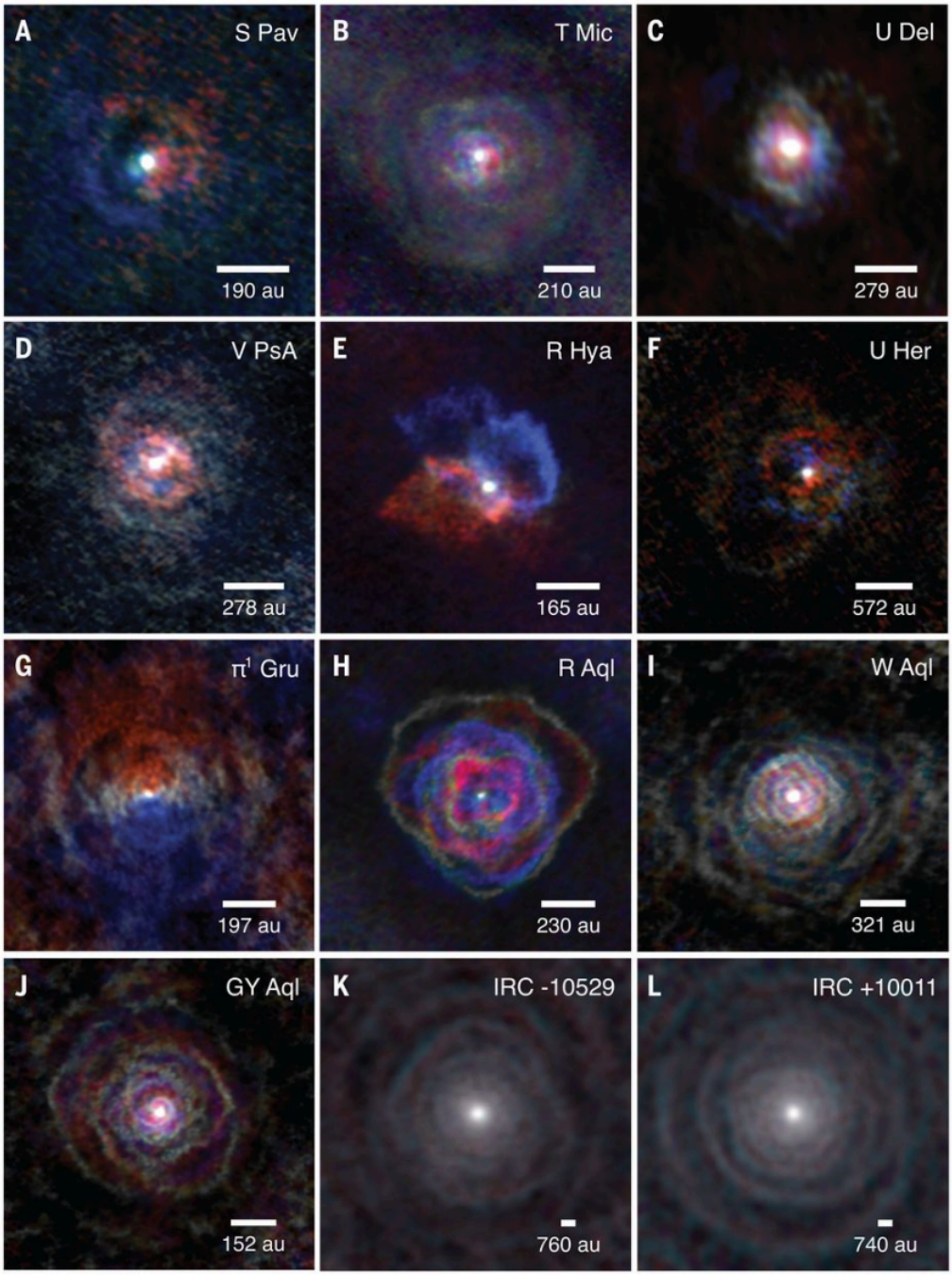

Figure 1.3: *Wind emissions of 12 AGB stars taken from* $^{12}CO\ J = 2 \rightarrow 1$ *transitions. Doppler shift shown in red and blue with rest velocity in white. Image credit: Decin et al., 2020*

It is from images such as these that work begins on analysing the spectroscopic output of the

Figure 1.4: *The carbon rich AGB star pictured here, CW Leonis, can be seen surrounded by the external layers of the CSE which have been shed through years of stellar wind driven mass loss. Image credit: ESA/Hubble, NASA, Toshiya Ueta (University of Denver), Hyosun Kim (KASI)*

stars giving line profiles as seen in Figure 1.5. It is profiles like this we will be modelling in this work in order to better understand the physical characteristics of the AGB star emissions.

1.3 Radiative Transfer Modelling

As seen above just looking at spectral line observations can reveal much about an AGB star but they do not reveal properties such as molecular distribution. To find these, a reverse modelling technique can be implemented by using a radiative transfer code on a model containing the necessary physical parameters to produce simulated line profiles that can be compared to the observational data.

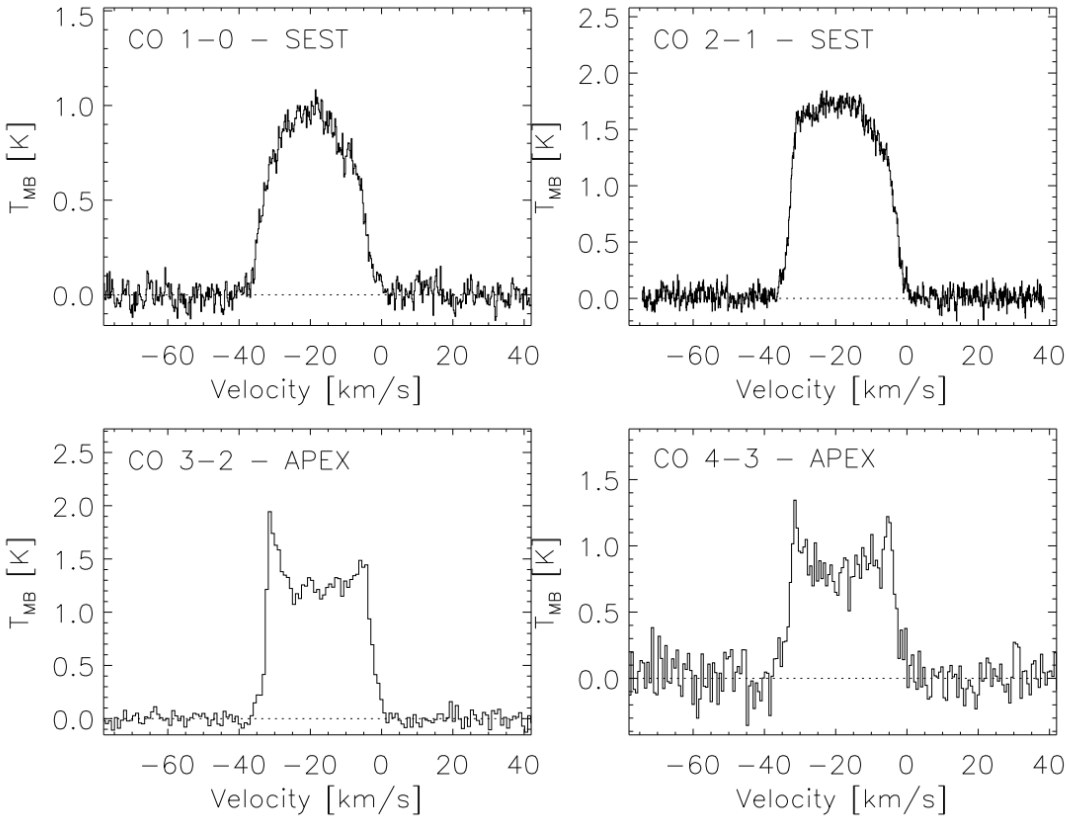

Figure 1.5: *^{12}CO line profile of R Scl across a number of transitional lines. Note how the parabolic shape weakens through the transitions as each following profile's transition is optically thinner than the preceding one revealing more of the structure (De Beck et al., 2010). This concept will be explored further in the following chapter.*

There are a number of codes available with different methods to solve radiative transfer equations such as GASTRoNOoM (Approximate Newton-Raphson operator) (Decin et al. 2006, Kim et al. 2010), LIME (accelerated Monte Carlo method) (Brinch & Hogerheijde, 2010), and MOLLIE (Accelerated Lambda Iteration) (Keto 1990, Keto & Rybicki 2010). Their use is to generate synthetic line profiles for comparisons with rotational transition lines from observations of various sources. The advantage to MOLLIE and LIME is that they are 3D radiative transfer codes. This allows for greater detail in the modelling of the outflow to give more accurate line profile models of sources.

MOLLIE uses an ALI algorithm that reduces the radiative transfer equations into a series of linear problems that can be solved quickly even under optically thick conditions (Rybicki & Hummer, 1991). The model is defined by several physical parameters; temperature, density, abundance, velocity, and turbulent velocity in addition to molecular data such as collisional

excitation rates. For some parameters such as density and temperature, power laws are used to represent the changes in value that can occur in the source while others can be held constant or modelled as shells. Some approximations can also be made to ensure smooth running of the code, in most cases regarding molecular clouds this is to assume a spherical shape but this can still produce accurate results (Carolan et al., 2009).

The model is then split into cells in a 3D grid before beginning the ALI to solve the equations. Figure 1.6 provides an example of how accurately source parameters can be modelled to reproduce observational data. A radiative transfer code such as MOLLIE has a variety of uses in the study of stars and interstellar objects such as chemical analysis of molecular clouds and their outflows (Rawlings et al., 2004). LIME runs similarly to MOLLIE in terms of the parameters and set up involved so offers a comparison for verifying models. It differs in that instead of splitting the model into a grid, it takes a random point distribution of intensities and the radiative transfer equations are then solved by use of the accelerated Monte Carlo method. These random cells have the advantage of bypassing the aliasing effects of the Cartesian grid.

The aim of this research is two-fold. The first is to assess the abilities of MOLLIE and LIME, both codes having been written to model molecular clouds, in modelling molecular AGB winds. Secondly to use one of these codes to model an example stellar wind system, IK Tau. Previous radiative transfer studies of AGB stars use 1D codes (Kim et al., 2010), so the use of these 3D codes and correctly modelling the mass outflow in three dimensions will provide a greater insight into how the envelope and ejecta of the star is developing as it approaches the PN stage.

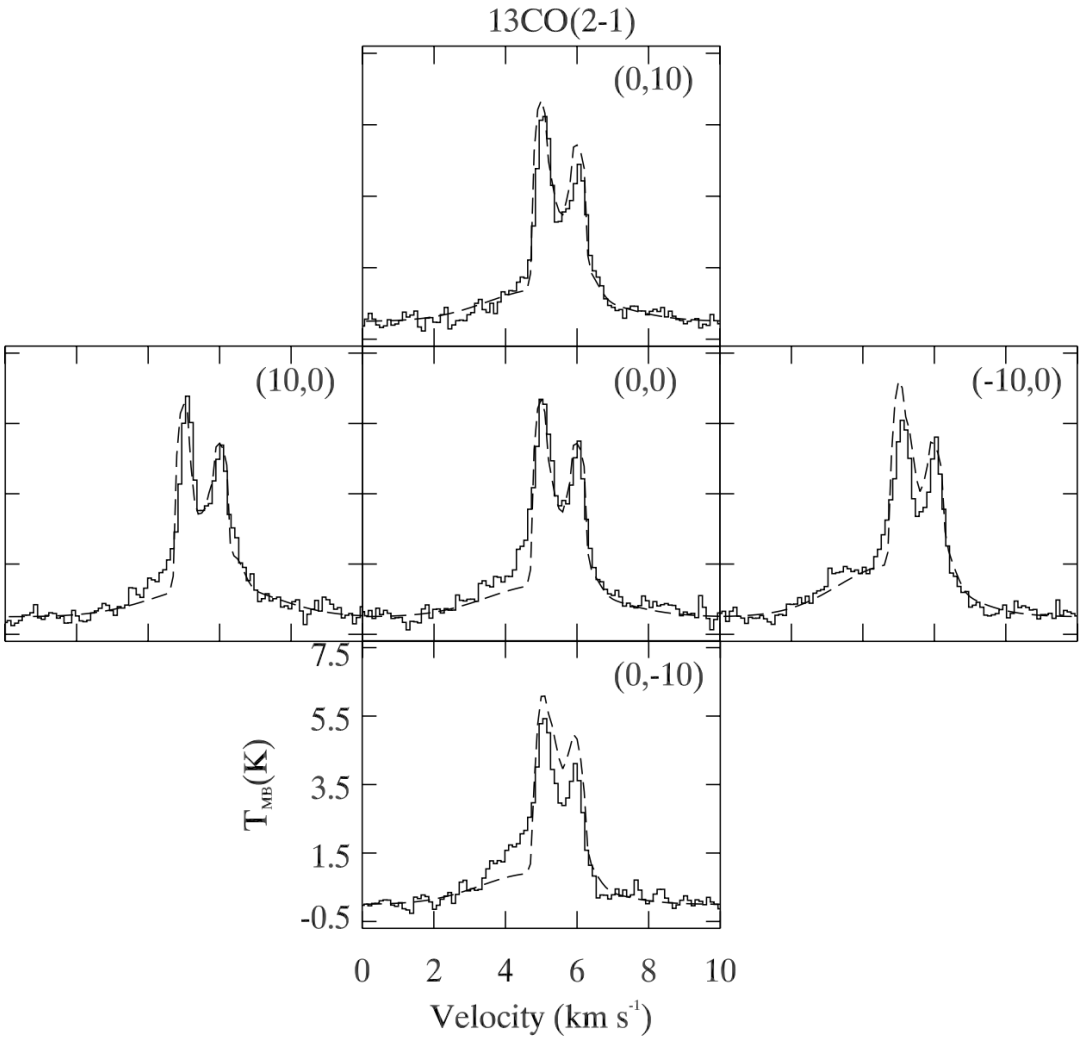

Figure 1.6: *Observed and modelled line profiles for* $^{13}CO\ J = 2 \rightarrow 1$ *of a cold dark molecular cloud. Observational data is the solid line, dashed lines give the modelled line profile (Carolan et al., 2007).*

CHAPTER 2

RADIATIVE TRANSFER

2.1 Introduction

Radiative transfer is the mechanism through which energy, such as electromagnetic radiation like light, is transferred in different mediums. This method is found in cold molecular clouds, the interstellar medium, and as demonstrated in this work, the circumstellar envelope of AGB stars and is illustrated schematically in Figure 2.1 and visually in Figure 2.2. As the radiation travels through a given medium, its intensity changes due to a number of factors such as:

- The properties of the medium the radiation travels through; density, temperature, and chemical composition
- The absorption or scattering of the radiation due to its incident angle upon the medium as well as the frequency of the radiation.
- Absorption and scattering also occurs due to the presence of obstacles (clouds or clumps possibly) within the medium

The radiative transfer equation is used to predict the change in intensity of the radiation these factors cause. In the case of AGB stars, solving the radiative transfer equation for a given molecule and transition line and through comparison with the observed line profile, gives the information on the physical conditions within the envelope of the star through study of observational profiles themselves.

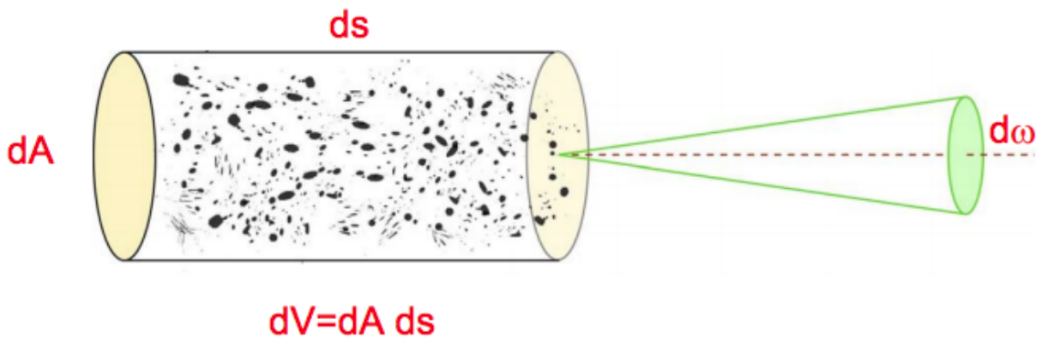

Figure 2.1: *Illustrated here is a ray dA, with a solid angle dω. The ray is travelling through a medium of length ds which consists of radiative absorbers and emitters. Credit: Mullins 2015*

2.2 The Radiative Transfer Equation

The intensity of a beam of radiation passing through an area of cloud or medium of length s and optical depth τ_ν can be given as I_ν. The beam intensity is given in units of

$$I_\nu \Rightarrow \frac{E}{t.\nu.\omega.A}$$

where E is the energy, t the time, ν the frequency, ω the angular area on the sky, and A the collecting area of the telescope observing the beam. As the beam passes through this medium, its intensity is changed by the absorption and emission within the cloud given by the absorption term α_ν (cm^{-1}), and the emission term j_ν ($\mathrm{erg\,s^{-1}\,cm^{-3}\,Hz^{-1}\,sr^{-1}}$). The α_ν term is the mean number of absorptions per centimetre throughout the medium, and j_ν is the radiation emitted per unit volume of the material. This change in radiation intensity can then be described as

$$I_\nu \rightarrow I_\nu + \mathrm{d}I_\nu$$

with

$$\mathrm{d}I_\nu = \mathrm{d}I_{\nu_{\mathrm{gain}}} + \mathrm{d}I_{\nu_{\mathrm{loss}}}$$

Now subbing in j_ν and α_ν, the equation becomes

$$\mathrm{d}I_\nu = j_\nu \mathrm{d}s - \alpha_\nu I_\nu \mathrm{d}s \tag{2.1}$$

Which can be rewritten as the radiative transfer equation

$$\frac{\mathrm{d}I_\nu}{\mathrm{d}s} = j_\nu - \alpha_\nu I_\nu \tag{2.2}$$

With this equation it is now possible to solve for an intensity which travels through a medium of emitters and absorbers. The two coefficients, j_ν and α_ν, once known, makes solving for the intensity straightforward. However, other physical conditions discussed below complicate the solution.

2.2.1 Analytic Solutions to the Radiative Transfer Equation

The solution to the radiative transfer equation has different forms depending on whether or not the medium is emitting, absorbing, or as above, both. In the case of a cloud which emits but does not absorb, $\alpha_\nu = 0$ and Eq. 2.2 becomes

$$\frac{\mathrm{d}I_\nu}{\mathrm{d}s} = j_\nu$$

Which when integrated gives

$$I_\nu = I_{\nu_0} + j_\nu s$$

which describes the increase of intensity of the beam equal to the emission coefficient along the line of sight. Whereas for a cloud which absorbs but does not emit, $j_\nu = 0$ and so Eq. 2.2 is then

$$\frac{\mathrm{d}I_\nu}{\mathrm{d}s} = -\alpha_\nu I_\nu$$

Which has the integrated solution of

$$I_\nu = I_{\nu_0} \exp\left[-\int \alpha_\nu s\right]$$

With this the intensity of the beam decreases by the exponential of the absorption coefficient integrated along the line of sight in the direction in which the beam travels.

The direction of line of sight along which a beam travels is an important factor to consider if instead of distance s, the optical depth τ_ν is used in its stead. This variable can be defined as:

$$\mathrm{d}\tau_\nu = \alpha_\nu \mathrm{d}s$$

or

$$\tau_\nu = \int \alpha_\nu(s)\mathrm{d}s$$

being the integrated absorption along the line of sight. There are two cases to consider with regards to optical thickness and radiative transfer. The first case is for $\tau_\nu >> 1$, a medium which is optically thick or opaque. The second type of medium is when $\tau_\nu << 1$ and is optically thin or transparent. Put into terms of a photon travelling through a medium, an optically thick medium is one in which an average photon would be unlikely to traverse the whole medium without being absorbed whereas the same photon travelling through an optically thin medium would likely traverse it without being absorbed.
Once again taking 2.2, and now dividing it by α_ν, gives the radiative transfer equation in terms of τ_ν,

$$\frac{\mathrm{d}I_\nu}{\mathrm{d}\tau_\nu} = S_\nu - I_\nu \tag{2.3}$$

where S_ν is the source function, defined in Eq. 2.4 below as the ratio of the emission coefficient to the absorption coefficient.

$$S_\nu = \frac{j_\nu}{\alpha_\nu} \tag{2.4}$$

A formal solution for 2.3 can be obtained with an integrating factor e^{τ_ν}

$$I_\nu = I_{\nu_0} e^{-\tau_\nu} \int_0^{\tau_\nu} S_\nu e^{(-\tau_\nu - \tau'_\nu)} \mathrm{d}\tau'_\nu \tag{2.5}$$

The equation can now be seen as the initial intensity or background radiation plus the integrated source or medium, both of which are diminished by absorption. For a constant source function, the equation takes the form:

$$I_\nu(\tau_\nu) = S_\nu + (I_{\nu_0} - S_\nu) e^{-\tau_\nu} \tag{2.6}$$

Consider now two extreme cases for optical thickness, $\tau_\nu \to \infty$ and $\tau_\nu \to 0$,

As $\tau_\nu \to \infty$, $I_\nu \to S_\nu$. In such an optically thick medium, the background radiation is omitted, so no information on the initial radiation is available.

As $\tau_\nu \to 0$, $I_\nu \to I_{\nu_0}(1-\tau_\nu) + S_\nu \tau_\nu$, In this extreme optically thin case, information on the background radiation is available as well as that attenuated by the medium itself.

Another determining factor is if the medium is in Thermodynamic Equilibrium (TE) or Local Thermodynamic Equilibrium (LTE). When the temperature of a cloud is constant throughout it, it is said to be in TE. While a cloud is in TE,

$$\frac{\mathrm{d}I_\nu}{\mathrm{d}s} = 0$$

and the Planck Function $B_\nu(T)$ is substituted for the intensity I_ν. Under this condition, Eq. 2.1 becomes

$$j_\nu - \alpha(\nu) B_\nu(T) = 0$$

This can then be rearranged into Kirchoff's Law

$$B_\nu(T) = \frac{j_\nu}{\alpha_\nu} \tag{2.7}$$

which is also the definition of the source equation S_ν. The implication of TE is that such a medium absorbs and emits each photon passing through it. That said, no TE clouds have been observed, although the cosmic microwave background acts as a blackbody in TE.

For LTE, the temperature is not constant but is assumed to remain constant over the distance travelled by the photon. So in this case each layer of the LTE approximation is defined by a separate blackbody to account for the change in temperature across the whole medium. While it is similar to TE where absorption and emission are in balance and $S_\nu = B_\nu(T)$, the intensity in LTE cases is not constant so Eq. 2.5 becomes:

$$I_\nu = I_{\nu_0} e^{-\tau_\nu} + B_\nu(T)(1 - e^{-\tau})$$

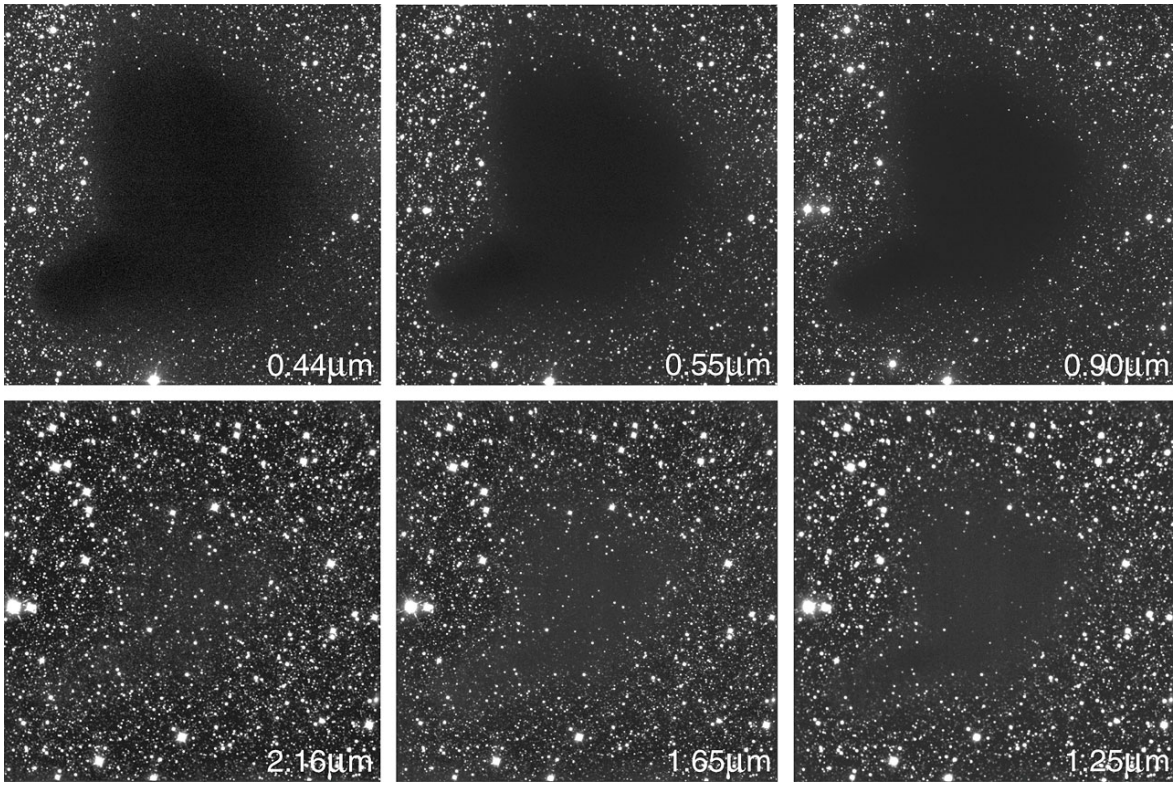

Figure 2.2: *Barnard-68 is a dense and optically thick molecular cloud. It is so dense it nearly appears as a hole in the sky as no light from stars behind it can penetrate the cloud. However, as the wavelength increases from optical to infrared, the cloud appears to recede and reveals the previously obscured stars (Alves, J. F. et al., 2001). Credit: ESO, https://www.eso.org/public/images/eso9934b/*

2.2.2 Numerical Solutions to the Radiative Transfer Equation

Along with solving the equation of radiative transfer, a radiative transfer code must also simultaneously solve the statistical equilibrium (SE) problems. An integral coefficient of the radiative transfer equation is the source function, S_ν. To calculate S_ν, the following equation is used:

$$S_{ij} = \frac{j_\nu}{\alpha_\nu} = \frac{n_i A_{ij}}{n_j B_{ji} - n_i B_{ij}} \tag{2.8}$$

where α_ν and j_ν are the absorption and emission coefficients as before. These coefficients depend on the populations of the upper (n_i) and lower (n_j) states and the Einstein coefficients (A_{ij}, B_{ij}, B_{ji}).

These coefficients, which are illustrated in Figure 2.3, were outlined by Einstein in his search for a microscopic relationship between emission and absorption as implied by Eq. 2.7, as follows:

1. Spontaneous Emission: Occurs when a system in level 2 drops to level 1 by emitting a photon. This can occur without a radiation field. Defined by the Einstein A-coefficient A_{21}

2. Absorption: Occurring only within a radiation field, a system in level 1 transitions to level 2 by absorbing a photon. Defined by the Einstein B-coefficient B_{12}

3. Stimulated Emission: A third process in which a system in level 2 is stimulated by a photon to emit another and drop to level 1. Defined by the Einstein B-coefficient B_{21}.

Here defined in terms of a system with levels 2 and 1, the coefficients can be used for any transition from level i to level j.

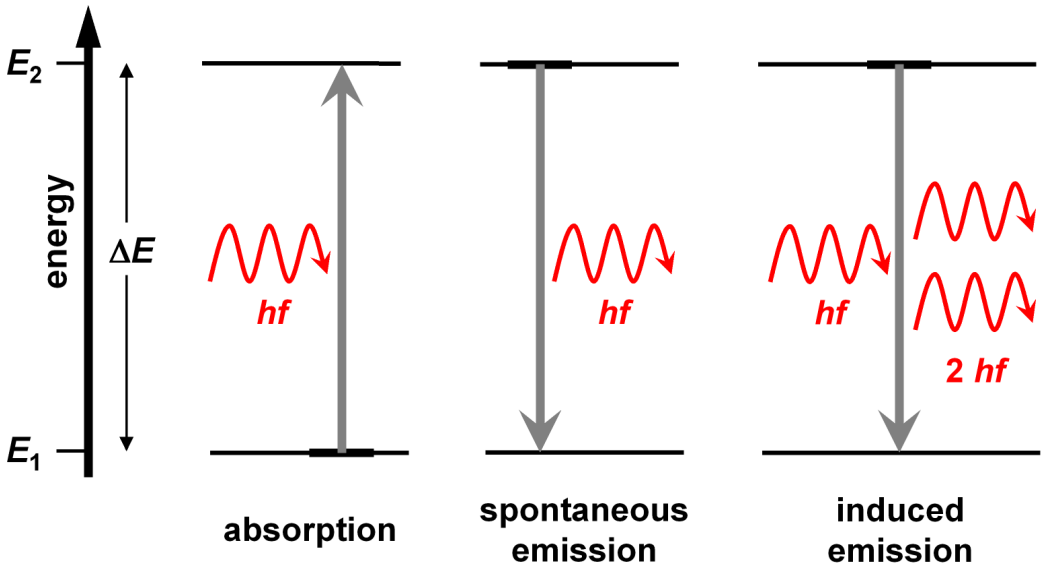

Figure 2.3: *The three main processes by which photons are absorbed or emitted from a two level atom as identified by Einstein. Credit: SEO Project, https://seos-project.eu/laser-rs/laser-rs-c02-p05.html*

The level populations are calculated by the SE

$$\sum_{j>1}[n_j A_{ji}+(n_j B_{ji}-n_i B_{ij})\bar{J}_{ji}]-\sum_{j<1}[n_i A_{ij}+(n_i B_{ij}-n_j B_{ji})\bar{J}_{ij}]+\sum_j[n_j C_{ji}-n_i C_{ij}]=0 \tag{2.9}$$

where $\overline{J_{ij}}$ is the mean intensity over the entire angle Ω in which the intensity is measured and given by

$$\overline{J_{ij}} = \frac{1}{4\pi} \int I_\nu(\Omega) \mathrm{d}\Omega \mathrm{d}\nu \tag{2.10}$$

and C_{ij} is the collisional rate coefficient of the molecules used.

Figure 2.4 displays the dependence that equations 2.5, 2.8, 2.9, and 2.10 have on each other and so requires a matrix with all variables at all locations to solve. As this is unfeasibly intensive, an iterative method is employed by codes following the steps outlined again in Figure 2.4 in order to solve the matrix.

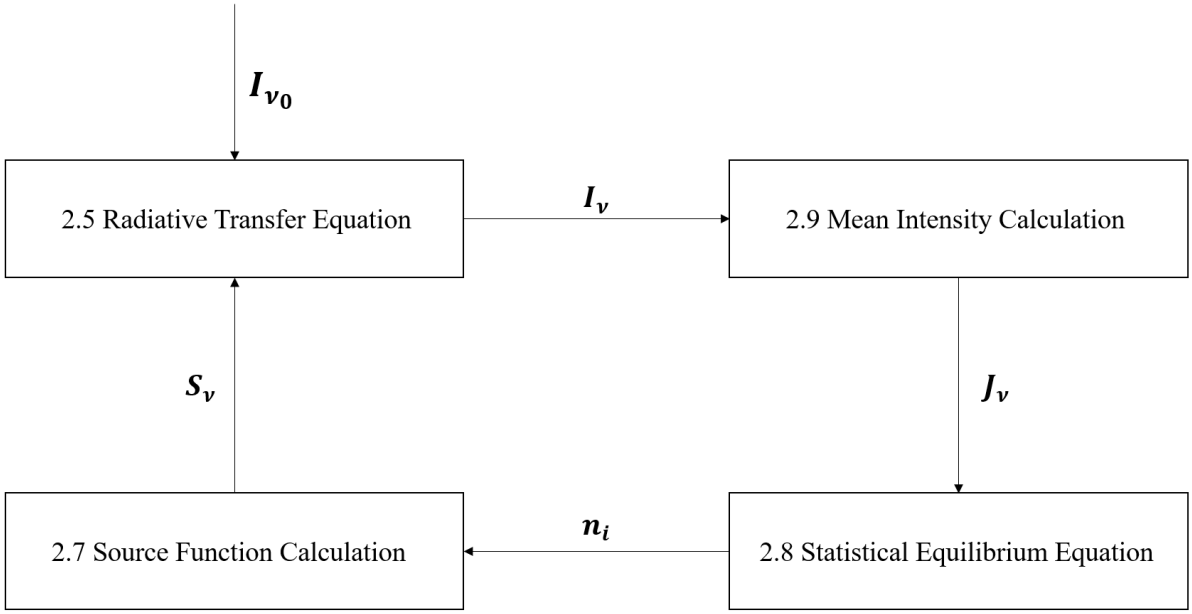

Figure 2.4: *The outline of the iterative process employed to solve the interdependence of the equations involved in solving the radiative transfer equation. Adapted from Zadelhoff et al. (2002)*

2.2.3 Accelerated Lambda Iteration

The first method by which the radiative transfer equation can be solved that is used in this work is the Accelerated Lambda Iteration (ALI) method. ALI is an improvement on lambda

iteration which is based on the use of the lambda operator Λ_{ij} as global matrix operator which acts upon S_ν, the source function, in order to calculate the mean intensity of a ray as it propagates through the grid cells.

$$\overline{J} = \Lambda_{ij}[S_{\nu_{ij}}] \tag{2.11}$$

With an initial assumption for the level populations, it follows the process outlined in Fig 2.4 to find the new level populations. It then runs iteratively until it reaches the point where the level populations fall beneath the convergence limit.

This method holds well for low optical thicknesses, where reaching the convergence limits for the level populations is a simpler task for photons with mean free path lengths between iterations of the calculation. For mediums with higher optical thicknesses however, the vastly increased number of iterations for a photon to travel the same distance as one in a low optical thickness medium means the time taken for notable changes in the level populations increase as well. Therefore lambda iteration is unfavourable due to how computationally intensive it can be in high optical density situations. Using a technique developed by Cannon (1973), Rybicki & Hummer (1991) sought a solution to these calculation times by splitting the lambda operator.

Instead of having the lambda operator act upon all points in the grid at once, the operator is split into its diagonal components Λ_{ij} and Λ^*_{ij}.

$$\overline{J} = (\Lambda_{ij} - \Lambda^*_{ij}) + \Lambda^*_{ij} \tag{2.12}$$

Here Λ_{ij} and Λ^*_{ij} are the exact and approximate operators respectively. Approximate operators, in this case Λ^*_{ij}, are easily invertible and so is used for the matrix inversion in the radiative transfer calculations. Now with Eq. 2.12, Eq. 2.11 becomes

$$\overline{J} = (\Lambda_{ij} - \Lambda^*_{ij})[S^\dagger_{\nu_{ij}}] + \Lambda^*_{ij}[S_{\nu_{ij}}] \tag{2.13}$$

where $S^\dagger$ is the source function of the previous iteration. This is then used in the statistical

equations to generate the new source function S_ν. The equation converges once $S_\nu = S_\nu^\dagger$ at which point the exact solution is known. By these means, the operator can change with the optical depth allowing for a much faster solution to be found in optically thick conditions.

2.2.4 Accelerated Monte Carlo

The second method for solving the radiative transfer equation is by Accelerated Monte Carlo (AMC). As in lambda iteration and ALI, AMC is an improvement over the standard Monte Carlo method for achieving convergence in optically thick conditions. Monte Carlo differs from lambda iteration where instead of following the path of a photon though the grid, the photon paths are randomly generated and the grid cells calculate the change in intensity for the photons that pass through it. One drawback of this method is that small cells can be missed in the sampling of photon paths, so care must be taken to ensure that all regions of the gridspace are adequately sampled by the randomly determined photon paths.

AMC approaches the issue of photons effectively becoming stuck in optically thick mediums in much the same way as ALI by splitting the mean intensity into the local (cell being sampled) and external (adjacent cells) contribution to radiation intensity.

$$\bar{J} = \left(\Lambda - \Lambda^*\right)\left[S^\dagger(\bar{J})\right] + \Lambda^*\left[S(\bar{J})\right]$$

$$\bar{J} = \bar{J}_{external} + \bar{J}_{local}$$

$$\bar{J} = \frac{1}{N}\sum_i I_{\nu_0,i}\, e^{-\tau_i} + \frac{1}{N}\sum_i S\left[1 - e^{-\tau}\right]$$

As before, $S^\dagger$ is the source function of the previous iteration and here N is the number of photons, and the equation is ran simultaneously with the SE equations in an iterative process until the population levels fall beneath the convergence limit (Zadelhoff et al., 2002).

2.3 Line Profile Formation

With the previous equations solved simultaneously, both radiative transfer codes then generate the line emission profile for the model. For this, the collision rate of the molecule in

question must be known either through observation or from a database. For this work, CO collisional rate coefficients were obtained from Yang et al. (2010) which is available in the Leiden Atomic & Molecule Database (Schöier et al. 2005).

The emission line is constructed about the central frequency where it is described by a gaussian profile

$$\phi(\nu) = \frac{1}{W\sqrt{\pi}} \exp \frac{-(\nu - \nu_0)}{W^2} \tag{2.14}$$

where $\phi(\nu)$ is the response profile function, the width about ν_0 where absorption and emission take place and W is the equation for the doppler broadening which includes both thermal and turbulent broadening

$$W = \left(\frac{\nu_0}{c}\right) \sqrt{v_{\text{turb}}^2 + \frac{2K_B T}{m}} \tag{2.15}$$

where T is the temperature of the system, K_B the Boltzmann constant, m the atomic weight of the molecule being studied, and v_{turb} is the turbulent velocity of the system. It is important to note here the greater effect on the outcome of line broadening that turbulence has over the temperature. In strong turbulent systems such as AGB outflows, the effect of thermal broadening was found to be almost negligible in comparison to the effect that the turbulent velocity had on the model. The expansion velocity also has an obvious effect on the profile, with slower systems such as molecular clouds having thinner profiles vs the generally broad, parabolic line emissions of AGB stars due to the higher velocities.

It is these fast moving outflows which also introduce asymmetrical structures into the line profiles. The inner hot gases can cause clumps, bulges, and other irregularities in an AGB star. These structures are often hidden by the optically thick outer CSE so either instruments with higher spatial resolutions (such as ALMA) or studies of optically thinner species are needed to reveal them. This can reveal what are known as soft parabolas (Olofsson et al. 1993) where the line profile takes on a shape as seen in Figure 1.5. A strong indicator of an asymmetrical outflow is a P Cygni profile. Named after the star in which the profile was first found, this can be seen in line emission profiles when the faster inner wind is accelerated through a slower moving wind and undergoes a degree of absorbtion within it.

These features within the line profiles are of interest due to the information they can reveal about the star or medium from which they were generated. We will now test two 3-D ra-

diative transfer codes with the goal of replicating observational data and the spectroscopic features therein.

CHAPTER 3

SELECTION & EVALUATION OF CODES

3.1 MOLLIE

The first of the two 3-D molecular line radiative transfer codes used in this work is MOLLIE (MOLecular LIne Explorer) developed by Keto & Rybicki (2010). Mollie is a radiative transfer code used to generate synthetic line profiles for comparison with rotational transition lines from observations of molecular clouds with varied properties such as cold massive cores(Carolan et al., 2009), starless cores (Keto & Caselli, 2008), and star forming regions (Loughnane et al., 2012).

MOLLIE uses an ALI algorithm (as outlined previously) that reduces the radiative transfer equations into a series of linear problems that can be solved quickly even under optically thick conditions (Rybicki & Hummer, 1991). The model itself is defined by several physical parameters; temperature, density, chemical abundance, velocity, and turbulent velocity in addition to molecular data such as collisional excitation rates. For some parameters, especially density and temperature, power laws can be implemented to calculate the change in value with distance or alternatively can be held constant or varying with shell depth. Some approximations can also be made to ensure smooth running of the code, in most cases regarding molecular clouds this is to assume a spherical shape but these approximations have little impact on the accuracy of the results (Carolan et al., 2007). The model constructed by these parameters is then split into cells in a 3D grid before beginning the ALI to solve the equations.

Due to its strong background in molecular cloud modelling and the comparable parameters with the CSE of AGB stars, MOLLIE was selected as the first code for this work to see if it was also capable of being used for the purpose of modelling AGB star outflows.

3.2 LIME

The second of the two 3-D molecular line radiative transfer equations used in this work is LIME (LIne Modelling Engine), written by Brinch & Hogerheijde (2010) and derived from the both 1 & 2-D code RATRAN (Hogerheijde & van der Tak, 2000). LIME is a hybrid code that uses the Monte-Carlo method to create unstructured 3-D cells by Delaunay triangulation for modelling the photon transport and then solves the population calculations using the ALI method. The benefit of the random grid cells produced by this method is that they bypass the aliasing effects of the Cartesian grid. See Figure 3.1 for a 2-D representation of the creation of grid cells from a random point distribution in LIME.

In terms of setting up the model, LIME is very similar to MOLLIE. The same physical parameters are in use here, although there is a change of units for LIME, using SI rather than CGS units. Once the gird is completed, the propagation of photons takes place along the Delaunay lines. This significantly decreases calculation times due to the fixed paths of the photons. This in combination with use of the ALI method for solving the radiative transfer equations gives LIME a much faster runtime than codes which solely use Monte-Carlo methods for both photon transport and equation solving.

As with MOLLIE, LIME was expected to be able to create models for a wide range of sources, so was used alongside MOLLIE in this section to determine their viability for modelling the CSE of AGB stars.

3.3 Test AGB Model

Before setting out to model the outflow of an AGB star, the two codes were compared using a test AGB model comprised of typical parameters for a star at this stage of its evolution. MOLLIE had already been shown to be very capable of modelling cold star forming regions but has yet to be used on evolved stars. As the physical parameters between these astrophys-

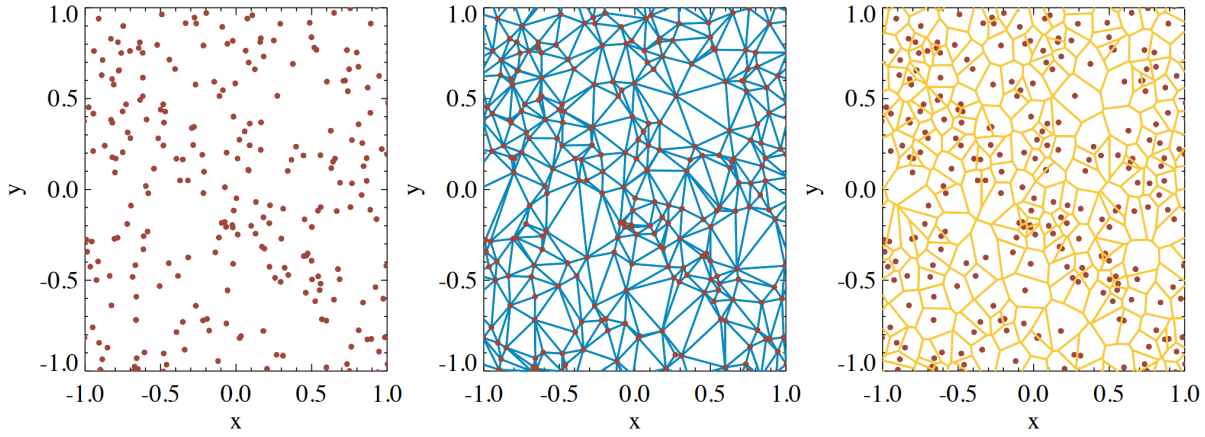

Figure 3.1: *From the left; random point distribution, Delaunay triangulation, and Voronoi tesselation to create the grid cells for the model. (Brinch & Hogerheijde, 2010).*

ical sources are compatible, it was thought that is would also be capable of modelling the outflow of an AGB star as well.

LIME has been used to study a variety of sources from protostar bipolar outflows by Bjerkeli et al.(2016) to the study the kinematics of a galactic merger by Wheeler et al. (2020), and, so LIME should prove to be able to handle modelling the outflow of an AGB.

3.3.1 Input Parameters

As mentioned above, a test model was made to compare results between the two codes. It was not necessary to use the observational data of a star at this stage as the objective was to determine the compatibility of MOLLIE and LIME rather than their accuracy vs observational data.

Parameters	**Model Inputs**
Density (kg m^{-3})	10.0×10^{-5}
Temperature (K)	230
Chemical Abundance (CO)	4.0×10^{-4}
Velocity (km s^{-1})	10
Turbulent Velocity (km s^{-1})	8, 5, 3, 1, 0.5

Table 3.1: *Parameters used for the test AGB model for both MOLLIE and LIME.*

As mentioned previously, MOLLIE and LIME use the same physical parameters, though

their units differ in MOLLIE using CGS and LIME SI. The parameters listed in Table 3.1 are given in SI for clarity. In testing the codes it was found when varying the turbulent velocity had a much greater effect on the compatibility of the codes and is presented here in the following section. The line profiles were viewed using CASA, (The CASA Team et al., 2001) and a synthisised beam of 6" was used for observing the line profiles of the two models. The profiles were then extracted and plotted using GNU Octave (Eaton et al, 2022).

3.4 Line Profile Comparison

Figure 3.2 shows the line profile of the test model with an 8 km s^{-1} turbulent outflow. The two codes show strong similarities here, both presenting a single peaked gaussian curve. However there is a small divergence that begins towards and following from the peak of the profile, but such minor differences are expected when modelling with two different codes (van Zadelhoff et al., 2006). Any finer structure that could be present in the line emission is blurred out due to the thermal broadening of the line by the high turbulent velocity of the outflow. There does remain a bulge on the red shifted side of the profile in both models that suggests there is additional structure that can be revealed with a lower turbulent velocity.

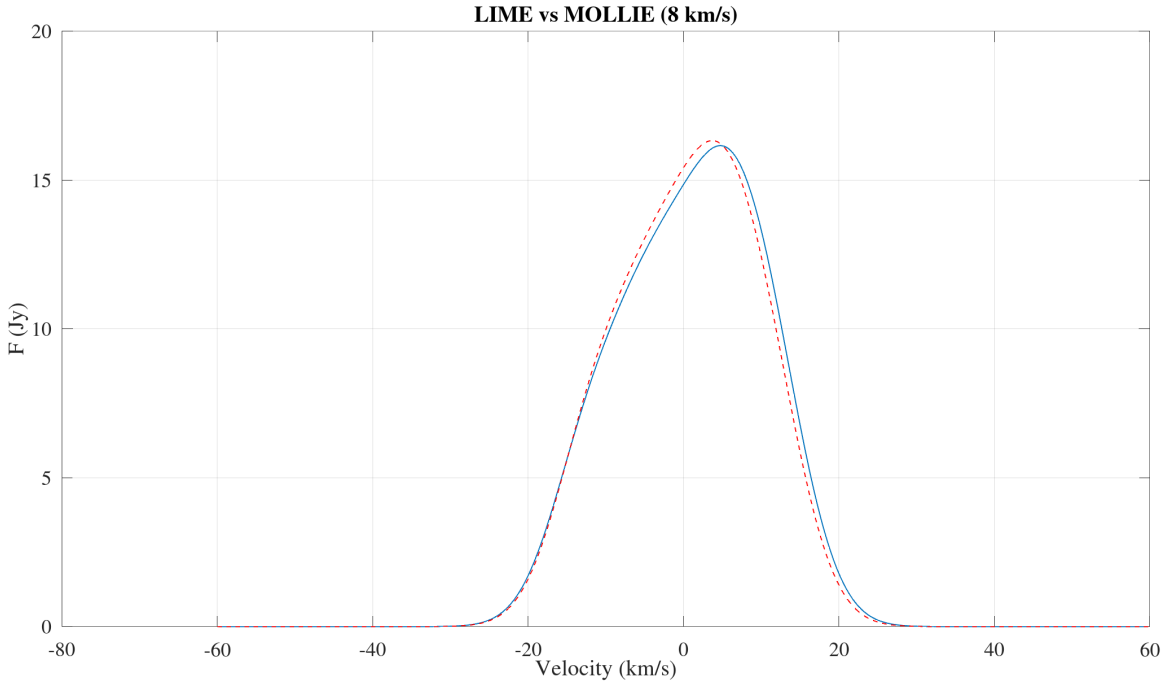

Figure 3.2: *8 km/s turbulent velocity comparison. The blue line is the LIME profile and the red dashed line is the MOLLIE profile.*

In Figure 3.3, we see immediately with a lower turbulent velocity of 5 km s^{-1}, the characteristic double peaked profile of an optically thin CSE begins to show in the two codes. Again they follow the same path towards the peak at which point they diverge with LIME having a lower intensity for the red shifted region and a greater degree of blue shift in the blue shifted region. Despite this the similarity between the codes is still strong at this stage.

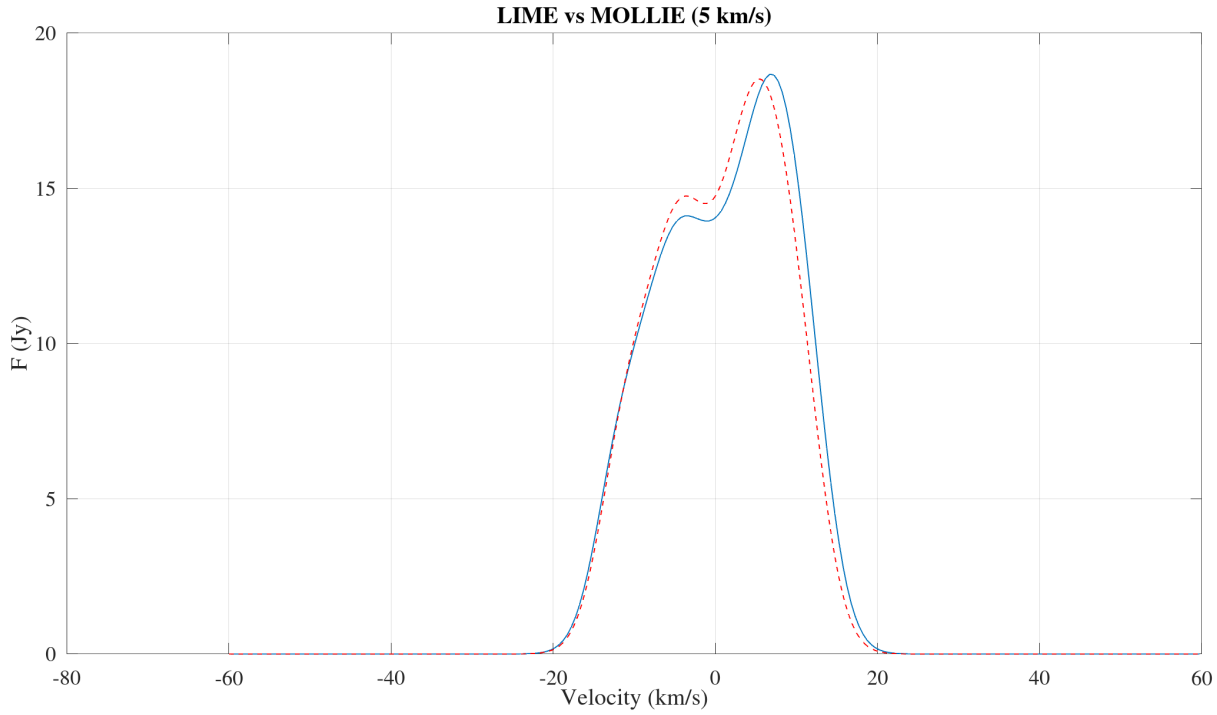

Figure 3.3: *5 km/s turbulent velocity comparison. The blue line is the LIME profile and the red dashed line is the MOLLIE profile.*

The increased definition of the double peaked profile continues in Figure 3.4 in which the models are set to a 3 km s^{-1} turbulent outflow velocity. Now we clearly see two distinct peaks emerging in the profile. However we also see yet further discrepancies between the codes following the same differences in the preceding plot with the LIME model having a lower intensity in the red shifted peak and higher then MOLLIE in the blue shifted side. MOLLIE also plots a deeper drop in intensity between the peaks

Now with a turbulent velocity of 1 km s^{-1} we see the MOLLIE model begin to break down.

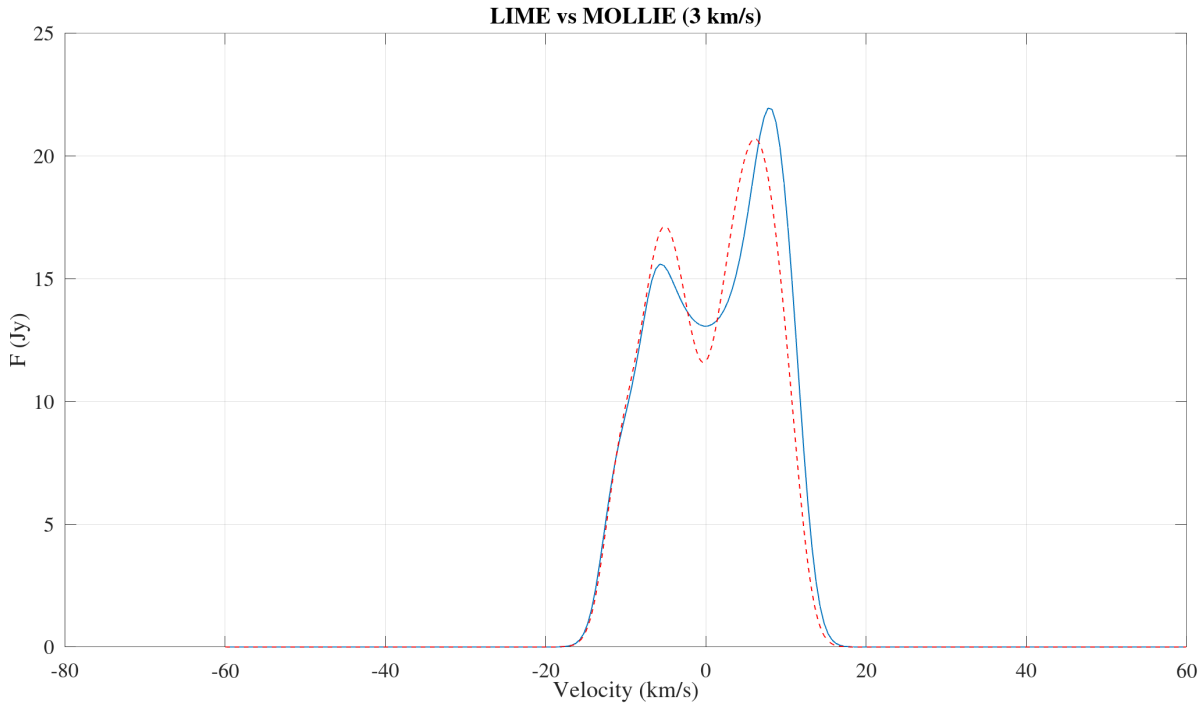

Figure 3.4: *3 km/s turbulent velocity comparison. The blue line is the LIME profile and the red dashed line is the MOLLIE profile.*

The plot is reasonable leading up to the peak however in the central region of the emission where an inverse parabolic curve is expected there is a sudden sharp drop in intensity and an unphysical mirroring within the curve itself. LIME continues to plot a good line emission, the peaks becoming narrower due to the much reduced thermal broadening effect of the low turbulent velocity vs the earlier models.

Finally at 0.5 km s^{-1} turbulent outflow velocity, the extent of MOLLIE's breakdown is observed in Figure 3.6. The line profile has been reduced to an almost symmetric jagged emission. The first peak at either end do follow the LIME model of the lower intensity on the red shifted side and similarly for the higher intensity on the opposite side, but whatever information in there is lost by the failing of the code as it moves towards the central regions and the peaks become mirrored. In this last plot LIME maintains the integrity of the model, clearly showing that it can handle a range of turbulent outflow velocities.

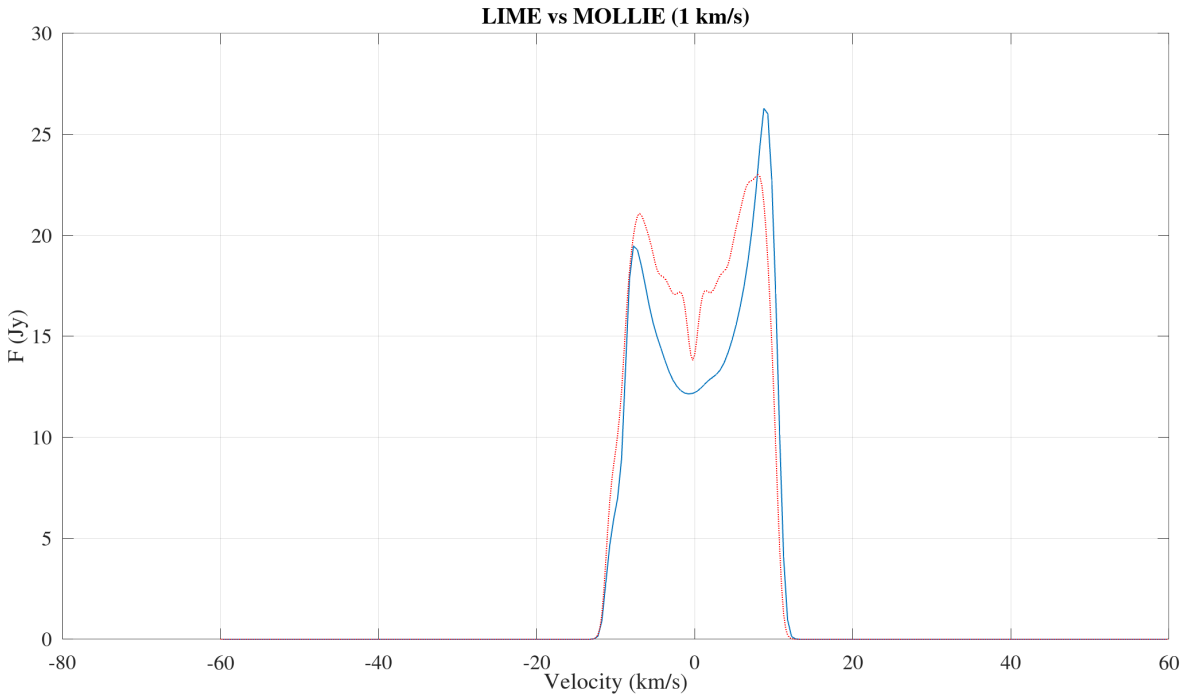

Figure 3.5: *1 km/s turbulent velocity comparison. The blue line is the LIME profile and the red dashed line is the MOLLIE profile.*

3.5 Discussion

In this chapter we have outlined two radiative transfer codes, MOLLIE and LIME, with different methods of tackling the radiative transfer equation in 3 dimensions. The codes were then tested with the characteristics of an AGB star to model its outflow. The line profiles of the model were then inspected using CASA.

At first both codes gave very similar outputs, a broad single peaked parabola which was to be expected from such a high turbulent velocity of 8 km/s broadening the line and obscuring detail. Only mild discrepancies are found between the two profiles, likely due to the differences in approaching gridding between MOLLIE's ALI and LIME's AMC methods. However as the turbulent velocity is lowered, with each subsequent model these discrepancies become more pronounced until the MOLLIE model completely fails at 0.5 km/s turbulent velocity.

The reason for this failure in MOLLIE with these parameter combinations is not obvious. A number of fixes were attempted, including increasing the resolution of the model, varying the number of velocity channels created, and varying the gaussian line widths used to assem-

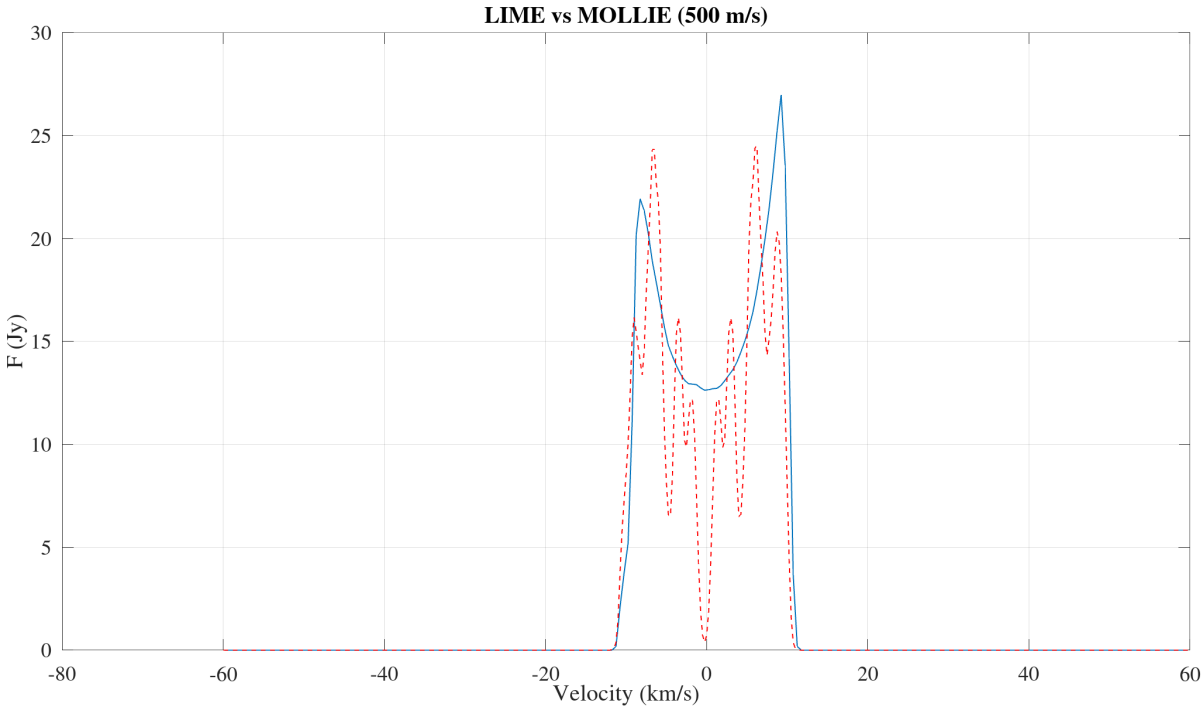

Figure 3.6: *0.5 km/s turbulent velocity comparison. The blue line is the LIME profile and the red dashed line is the MOLLIE profile.*

ble the line profile. As the numerical error persisted in all cases, this points to a failure in the algorithm for the radiative transfer, or the ray-tracing calculation for the line profile. Fixing either of these possible issues is beyond the scope of this work but these investigations did make it at least possible to identify the parameter combinations that cause the code to fail: which is when the bulk velocity exceeds the turbulent velocity by a factor of about 10. This condition is rarely seen in collapsing star forming conditions (see Figure 1.6 in comparison to the profiles modelled in this chapter, particularly with regards to the much lower expansion velocities of molecular clouds), except perhaps in bipolar jets, however for the AGB wind systems studied here these conditions are common. Therefore MOLLIE is clearly not suitable for modelling these systems and all further work in this project is undertaken with LIME.

CHAPTER 4

IK TAURI

4.1 The Source

The star of interest to this project is IK Tauri (henceforth IK Tau), also known as NML Tauri after its discovery by Neugenbauer et al. (1965). This highly-red AGB star is a Mira type variable that's rich in oxygen. Its period is estimated at ~460 days with brightness variations in the V-band of ΔV~6 mag (Wong et al., 2018). The spectral type of IK Tau ranges from M8 to M11 (Kharchenko & Roeser, 2009) with estimates for the distance being given from 250pc (Olofsson et al., 1998) up to 284pc from the Gaia collaboration (Brown et al., 2018). The mass loss rate estimations of IK Tau are high for an AGB star, ranging from ~3.8×10^{-6} $M_{\odot}\mathrm{yr}^{-1}$ (Neri et al., 1998) to ~4.7×10^{-6} $M_{\odot}\mathrm{yr}^{-1}$ (Kim et al., 2010).

This star was chosen due to the high quality of observational data with which to compare model outputs and that the CSE is spherically symmetric in shape. The relative proximity of IK Tau combined with its high mass loss rate has made it the ideal target for molecular emission line studies. This allows for the use of observations that have data for several CO isotopologues and transition lines. From these differences in abundance and optical depth of the isotopologues or transitions lines, the CO and therefore the H_2 can be traced over a wide range of physical conditions.

Data for analysis and model verification was adapted from de Beck et al. (2010), using the James Clerk Maxwell Telescope (JCMT) and Castro-Carizzo et al. (2010) with the Institut

de Radioastronomie Millimetrique (IRAM) interferometer in combination with the IRAM 30-metre telescope. See Figures 4.1 and 4.2 for this data respectively. A radiative transfer model was constructed to produce synthetic line emissions for the purpose of comparison with the adapted data. Estimations for the temperature, velocity, and the physical model (distance and radius) were constrained using literature. The density and chemical abundance were found through an iterative approach, where each model was evaluated on the quality of the fit and how this has changed from the previous model. The process was then repeated with new parameters until a model that best agreed with observational results was achieved. Another option would be to run a vast number of models that would cover all possible parameters and then measuring the deviation from the data, find the statistical minimum. However, this is difficult to do in practice.

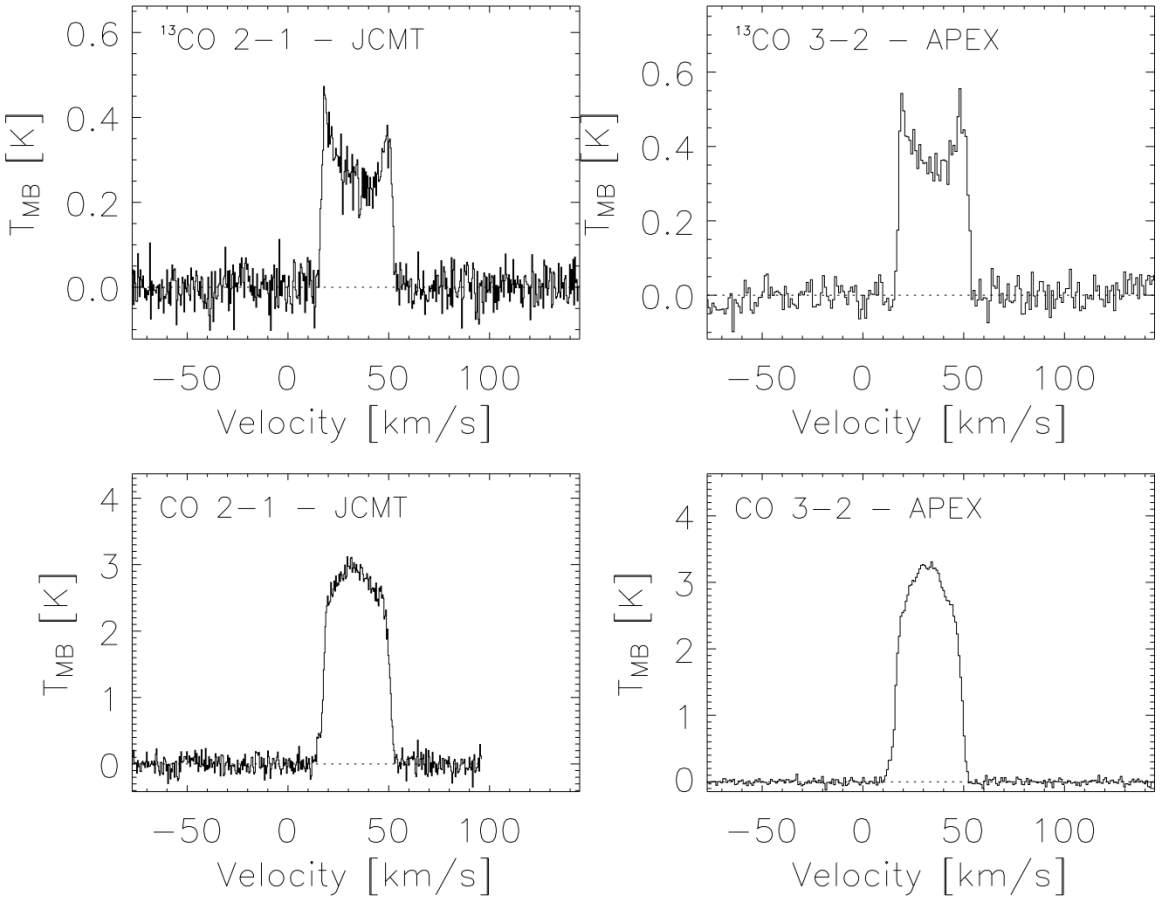

Figure 4.1: *The ^{12}CO lines (here labelled as CO) are more parabolic in shape than the ^{13}CO. Caused by a lower abundance in ^{13}CO giving an optically thinner profile. (De Beck et al., 2010).*

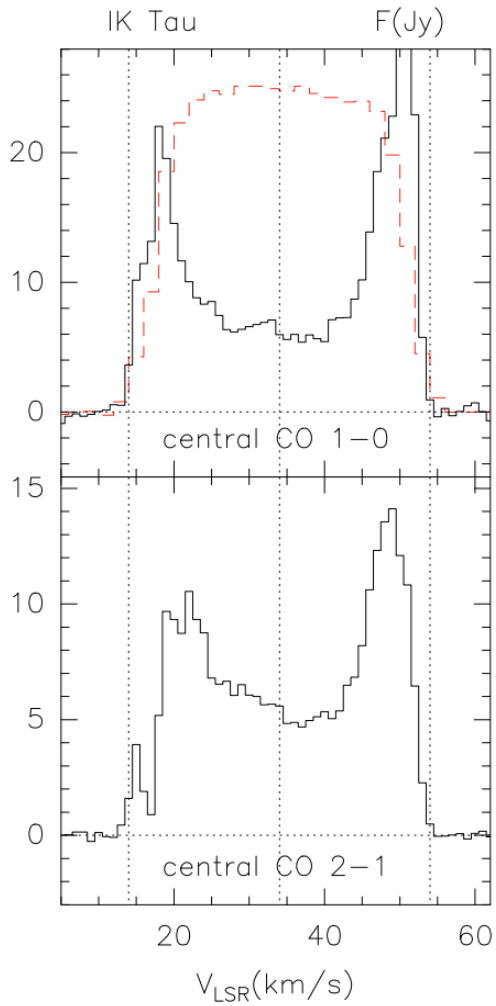

Figure 4.2: *Spectra of the center region of IK Tau given by solid lines. The dashed lines are obtained by spatially integrating over the emission region. (Castro-Carrizo et al., 2010).*

4.2 Input Parameters

The structure of an AGB's circumstellar envelope can be complicated due to of factors such as stellar wind bow shocks, either in the global flow or localised around clumps in the wind, as well as intermittent mass-loss events, and bipolar outflows, The excitation of molecules affecting the heating and cooling process as well as various grain size distributions can also attribute to the intricacy of an envelope. These factors can quickly over-complicate a model so for streamlining assumptions can be made when attempting a radiative transfer model. In this case, IK Tau is treated as having a uniform spherical envelope expanding with a constant velocity and no irregularities to its mass loss rate.

As such, the model is constrained by the same parameters as used in the previous test models; H_2 density, temperature, chemical abundance of the trace molecule (CO once again for stated reasons), expansion velocity, and turbulent velocity which shall be outlined as follows and presented in Table 4.1.

Parameters	**Model Inputs**
Density (kg m^{-3})	8.0×10^{-5}
Temperature (K)	670
Chemical Abundance (^{12}CO, ^{13}CO)	6.0×10^{-4}, 1.5×10^{-5}
Velocity (km s^{-1})	18
Turbulent Velocity (km s^{-1})	1

Table 4.1: *Parameters used for the model of IK Tau.*

4.2.1 Density & Temperature

The density of a star can be considered a free parameter as with the findings of Boulangier et al. (2019), and present a range of stellar densities from 10^{-8} to 10^{-4} kg m^{-3}, obtained either through calculations or modelling. The H_2 density used in this work was constrained after a number of iterations using these ranges as a guide, before the best fit value of 8×10^{-5} kg m^{-3} was found. The density follows an r^{-2} falloff dictated by the conservation of mass which is valid for a CSE expanding at a constant velocity.

The kinetic temperature of the gas was described by the following power law:

$$T(r) = T(r_0)\left(\frac{r_0}{r}\right)^{-\alpha} \tag{4.1}$$

Where $T(r_0)$ = 2667 K for a distance of 260pc and $r_0 = 3.14\times10^{13}$ (de Beck et al., 2010), α may range between 0.4 and 0.7 (Cherchneff et al. 1992) and so 0.6 was used in accordance with Decin (2010). This gives an initial value of 670 K for T(r), which cools exponentially to the cosmic microwave background.

4.2.2 Chemical Abundance

The chemical abundance of a molecule is defined as being a ratio with respect to the abundance of molecular hydrogen. A wide range of observational and theoretical predictions exist for the chemical abundances of IK Tau. The ^{12}CO abundance is often in the order of

10^{-4} and the ^{13}CO abundance is a factor of 10 lower in most cases at 10^{-5} or possibly as low as 10^{-6} (Decin et al., 2010). For this work, values of 6×10^{-4} for the ^{12}CO abundance and 1.5×10^{-5} for the ^{13}CO abundance were selected which both fall within accepted values for the chemical abundance.

4.2.3 Velocity & Turbulent Velocity

The expansion velocity for IK Tau's wind range from 17.1 to 18.5 km s^{-1} (Decin et al. 2010, de Beck et al. 2010), with the systemic velocity with respect to the local standard of rest being ~V_{sys}^{LSR} 32-34 km s^{-1} (Duari et al. 1999, Kim et al. 2010). Adopting a V_{sys}^{LSR} of 32 km s^{-1}, the expansion velocity was constrained to be 18 km s^{-1}.

For the turbulent velocity a number of values were used by the same method as the test models to determine the best fit for the line profiles. A v_{turb} of 1 km s^{-1} was found to sufficiently broaden the profile in agreement with the adapted data.

4.3 Line Profile Results

4.3.1 ^{12}CO $J = 1 \rightarrow 0$

Figure 4.3 displays the observed ^{12}CO(1-0) rotational transition line of IK Tau with a dashed red line and the simulated line profile modelled in LIME in solid blue. The data adapted from Castro-Carizzo et al. (2010), was a result of combined spectra from the IRAM Plateau de Bure Interferometer and IRAM 30m telescope. The beam size was 4".0 × 3".1 and gives a characteristic double peaked profile. While such a profile is often the result of low optical thickness, an instrument with a sufficiently high spatial resolution has the capability to resolve the separate peaks of a profile even at relatively high optical depth.

The LIME model reproduces shape of the profile and peak flux intensity well, as well as the slight asymmetric broadening of the two peaks. The broader blueshifted side of the observed profile could be accounted for by a warmer inner region's emission being absorbed by cooler gas in the outer layers of the CSE. This gas, moving slightly faster than the outermost components, could introduce a bulge in the envelope, introducing asymmetry to an otherwise spherical CSE.

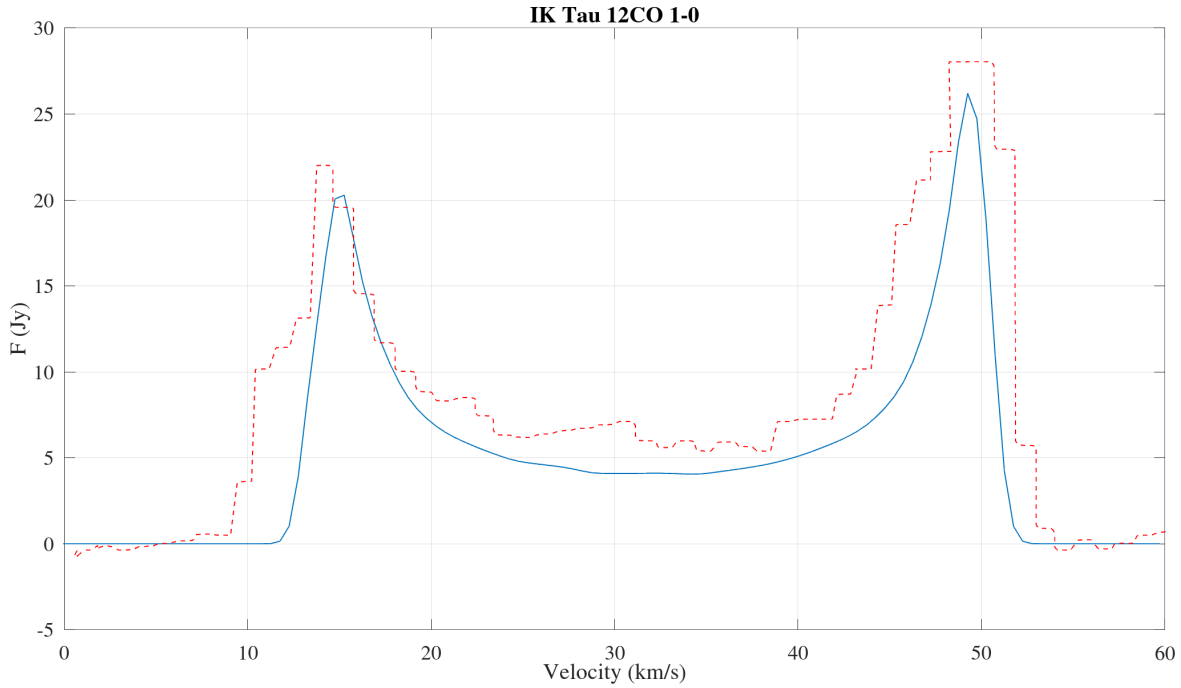

Figure 4.3: *^{12}CO(1-0) modelled line profile and observed line profile adapted from Castro-Carrizo et al., (2010). Modelled profile presented in blue, adapted data by the red dashed line.* $\sigma = 0.5$ *Jy*

4.3.2 ^{12}CO $J = 2 \rightarrow 1$

The first of the ^{12}CO(2-1) line profiles is shown in 4.4. This profile, adapted from de Beck et al. (2010), was taken with the JCMT and a beamsize of 20"× 20". The result of which is a lower resolution spectrum with a parabolic shape to it as would be expected for a high abundance molecule like ^{12}CO which would have a high degree of optical thickness. The LIME model successfully traced the observed profile at this large beam size of 20" × 20".

The beam size was then dropped to 1".6 × 1".1 for the IRAM data in Figure 4.5. Here the evidence of the self absorption can be seen in greater detail in the observed profile but is not fully replicated in the simulated profile. There is a minor bulge in the LIME generated profile at ~14 km s^{-1}, which grows more pronounced at lower turbulent velocities where the reduced broadening due to turbulence doesn't absorb the feature into the main blue shifted peak itself. Otherwise the model holds the overall shape well, with the blue shifted peak remaining broader than the red, although the intensity is generally greater across the line.

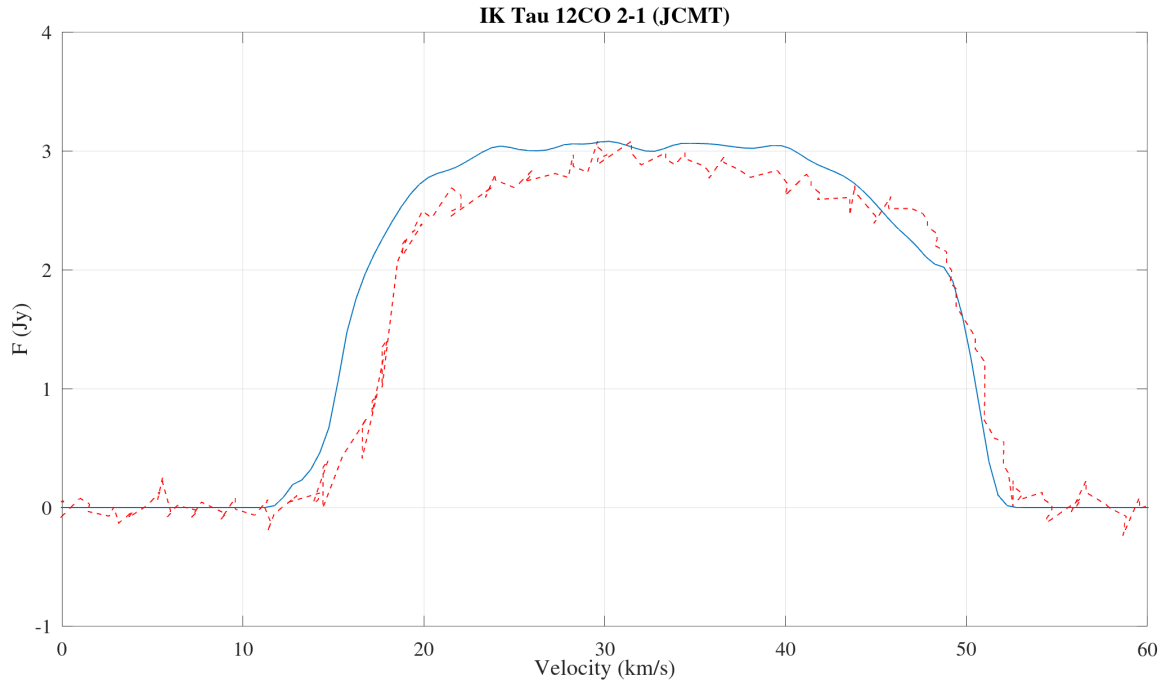

Figure 4.4: *^{12}CO(2-1) modelled line profile and observed line profile adapted from de Beck et al., (2010). Modelled profile presented in blue, adapted data by the red dashed line. $\sigma = 0.25$ Jy*

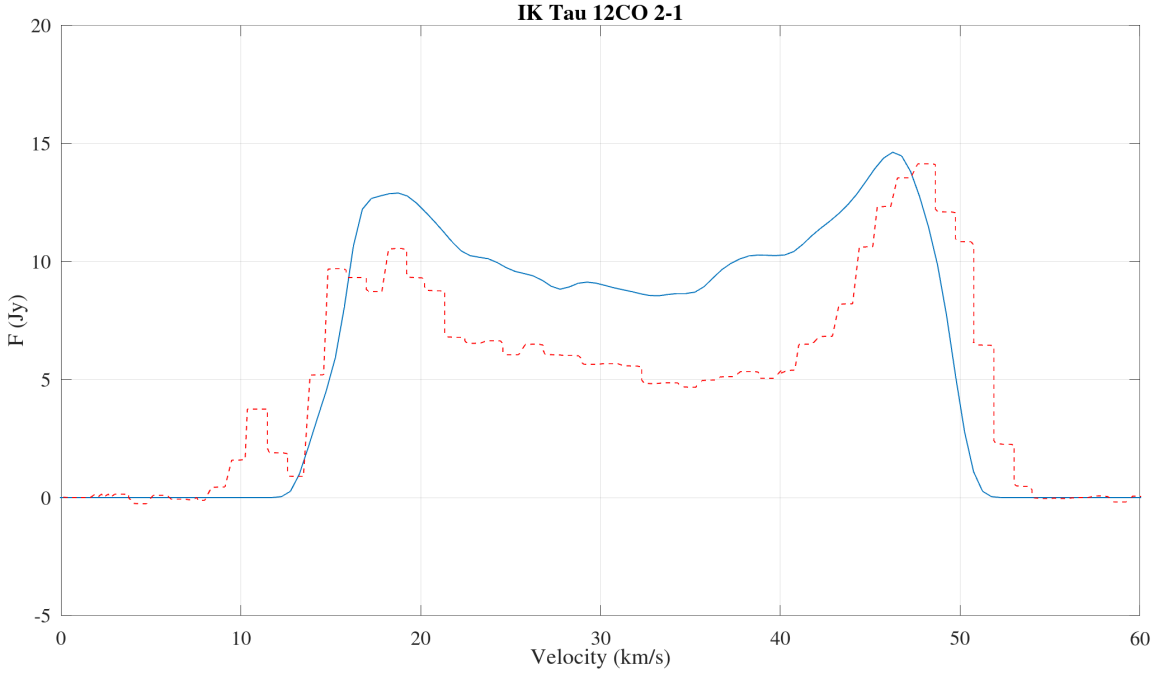

Figure 4.5: *^{12}CO(2-1) modelled line profile and observed line profile adapted from Castro-Carrizo et al., (2010). Modelled profile presented in blue, adapted data by the red dashed line. $\sigma = 0.4$ Jy*

4.3.3 ^{13}CO $J = 2 \rightarrow 1$

The final figure, Figure 4.6, shows the ^{13}CO(2-1) complement to 4.4. What is immediately apparent is the greatly reduced intensity and twin peaked or soft-top gaussian shape compared to the parabolic ^{12}CO line. ^{13}CO has a much lower abundance than that of ^{12}CO leading to very thin lines and allows for resolved peaks even at the low resolution of the JCMT. The modelled profile is similarly thin due to the reduced abundance and follows the now higher intensity blue shift peak down to the reduced red.

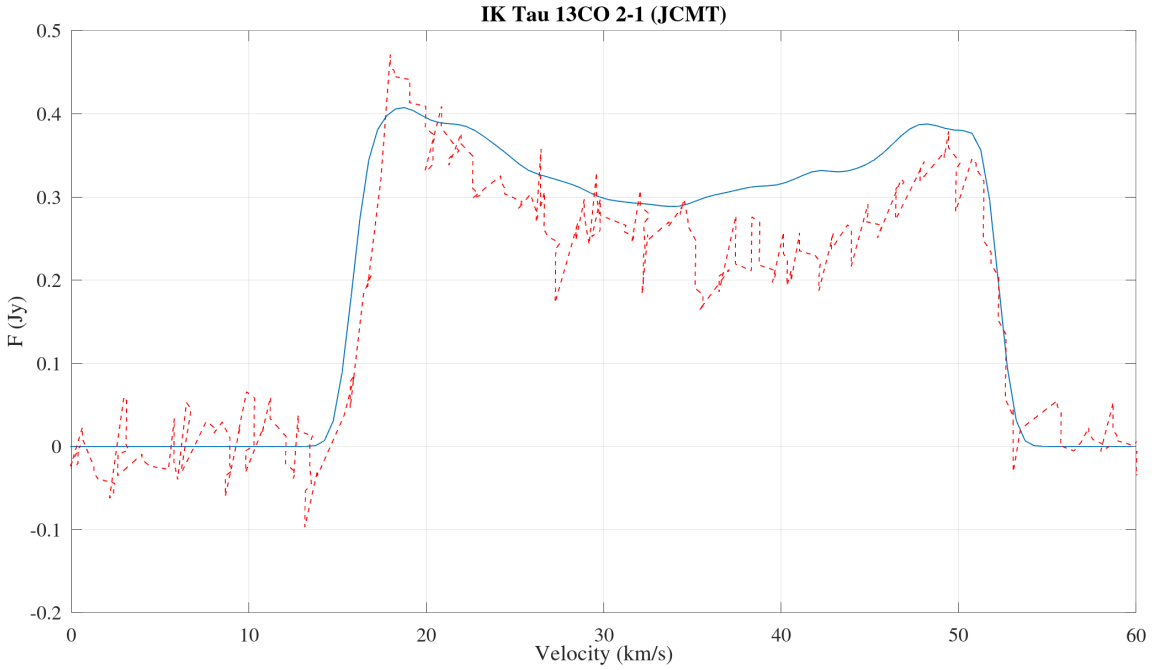

Figure 4.6: *^{13}CO(2-1) modelled line profile and observed line profile adapted from de Beck et al., (2010). Modelled profile presented in blue, adapted data by the red dashed line. $\sigma = 0.05$ Jy*

4.4 Discussion

In this chapter the 3-D radiative transfer code LIME was used to model the outflow of the AGB star IK Tau. The line emissions for two common molecular species, ^{12}CO and ^{13}CO, were modelled in a variety of resolutions and transitional lines, each giving a different perspective on the dynamics of the CSE of IK Tau.

As mentioned previously, with their high abundance, optically thick species such as ^{12}CO and ^{13}CO make ideal tracers of H_2 gas in an AGB star. This high abundance means the

molecules can be found throughout the entire CSE and so gives information from the core to the extremities of the gaseous envelope. It is towards the edge of the envelope where evidence of self-absorption in the ^{12}CO (2-1) line but due to the broadening of the turbulence and the relative simplicity of the model, this possible bulge in the CSE could not be resolved in greater detail at this time. Future work could attempt to resolve this feature through the use of splitting the model into multiple shells to give greater control over the density, temperature, and abundance in specific areas of the CSE.

This aside, we can assert the models give a satisfactory fit to the line profiles from both the JCMT and IRAM data, with the exception of Figure 4.5. Here it proved harder to capture both the asymmetry in the line profile and the depth of the central absorption, resulting in a slightly poorer fit than for the other datasets. From the accuracy of the ^{12}CO and ^{13}CO we have justified both the parameters from literature and those constrained within this work for these observations of IK Tau, This shows that with a model that does not include complexities within the medium, the 3-D radiative transfer code LIME can achieve accurate results.

CHAPTER 5

CONCLUSIONS AND FUTURE WORK

The aim of this work was to test the use of 3-D radiative transfer codes in the modelling of an AGB star. Of the two codes used, MOLLIE was found to be unsuitable for use with the parameters necessary for these conditions. The numerical error causing the failure in line profile creation persisted across attempted fixes and so the code was not used for further modelling in this research. LIME ran without any failures for every given turbulent velocity value and behaved as expected for those inputs, the line profile getting increasingly thinner and sharper as the broadening due to turbulence decreased. Going forward to modelling data from the AGB source IK Tau, LIME proved it could be used to replicate observations from two telescopes at various transition lines and molecular species. Using CO as a tracer for the model, we have a strong indicator for most of the CSE. However, there are some structures such as the self-absorption in the ^{12}CO (2-1) line which did not come through in this model. This may also be in part to deviations from the spherical symmetry within the star such as from clumps, bulges, spirals, bipolarity or any other structures which can affect the outflow of a star.

Considering future work, with better data from increasingly more powerful telescopes a more complex model could be constructed to bring out the structures in the CSE. However producing such a model would likely be an incredibly time-consuming affair so another tool which could prove useful in the study of AGB stars is SHAPE (Steffen et al. 2011). SHAPE is a 3-D modelling tool most often used in the study of nebulae (Clyne et al. 2005), but as with the hypothesis for using these codes with AGB parameters, SHAPE could be used to

model the finer structures of an AGB's CSE. This can be done in conjunction with shapemol (Santander-Garcia et al. 2015). Shapemol performs molecular radiative transfer for models in Shape, but is only suitable for optically thin cases so would be unsuitable for the sole method of analysis for an AGB star. However, as Shape defines the density, temperature, and velocity for each datapoint in the model, and shapemol the molecular abundance and turbulent width, these could be exported to LIME for a more comprehensive radiative transfer analysis. Using Shape and shapemol in this way would remove much of the tedium involved with constraining ever more complex models for ever more detailed, high resolution images. Through the successful modelling of these structures, a better understanding of how these irregularities influence the shape of the CSE and the planetary nebula that would follow after.

REFERENCES

Alves J. F. et al., *"Internal structure of a cold dark molecular cloud inferred from the extinction of background starlight"*, Nature, vol. 409, pp. 159, (2001).

Bjerkeli P. et al., *"A young bipolar outflow from IRAS 15398-3359"*,Astronomy & Astrophysics, vol. 587, pp. A145, (2016).

Bot C. et al., *"Millimeter dust continuum emission revealing the true mass of giant molecular clouds in the Small Magellanic Cloud"*, Astronomy & Astrophysics, vol. 471, pp. 103-112, (2007).

Boulangier J. et al., *"Developing a self-consistent AGB wind model – I. Chemical, thermal, and dynamical coupling"*, Monthly Notices of the Royal Astronomical Society, vol. 482, pp. 5052-5077, (2018).

Brinch C. and Hogerheijde M. R., *"LIME – a flexible, non-LTE line excitation and radiation transfer method for millimeter & far-infrared wavelengths"*, Astronomy and Astrophysics, vol. 523, p. A25, (2010).

Burke B. F. and Graham-Smith F., *"An Introduction to Radio Astronomy, 3rd ed."*, Cambridge: Cambridge University Press, (2009).

Cannon C. J., *"Frequency-Quadrature Perturbations in Radiative-Transfer Theory"*, The Astrophysical Journal, vol. 185, pp. 621-630, (1973).

Carolan P. et al., *""CO abundances in a protostellar cloud: freeze-out and desorption in the envelope and outflow of L483""*, Monthly Notices of the Royal Astronomical Society, vol. 383, no. 2, pp. 705-712, (2007).

Carolan P. et al., *"Supersonic turbulence in the cold massive core JCMT 18354-0649S*, Monthly Notices of the Royal Astronomical Society, vol. 400, no. 1, pp. 78-89, (2009).

The CASA Team et al., *"CASA, the Common Astronomy Software Applications for Radio Astronomy"*, Publications of the Astronomical Society of the Pacific, 134, 114501. DOI: 10.1088/1538-3873/ac9642, (2001).

Castro-Carrizo A. et al., *"Mapping the* $^{12}CO\ J = 1 \rightarrow 0$ *and* $J = 2 \rightarrow 1$ *emission in AGB and early post-AGB circumstellar envelopes"*, Astronomy & Astrophysics, vol. 523, p. A59, (2010).

Clyne N. et al., *"A morpho-kinematic and spectroscopic study of the bipolar nebulae: M 2-9, Mz 3, and Hen 2-104"*, Astronomy & Astrophysics, vol. 582, pp. A60, (2006).

Danilovich T. et al., *"Rotational Spectra of Vibrationally Excited AlO and TiO in Oxygen-rich Stars"*, The Astrophysical Journal, vol. 904, p. 110, (2020).

De Beck E. et al., *"Probing the mass-loss history of AGB and red supergiant stars from CO rotational line profiles"*, Astronomy & Astrophysics, vol. 523, p. A18, (2010).

Decin L. et al., *"Probing the mass-loss history of AGB and red supergiant stars from CO rotational line profiles"*, Astronomy & Astrophysics, vol. 456, pp. 549-563, (2006).

Decin L. et al., *"Circumstellar molecular composition of the oxygen-rich AGB star IK Tau: II. In-depth non-LTE chemical abundance analysis"*, Astronomy & Astrophysics, vol. 516, pp. A69, (2010).

Decin L. et al., *"(Sub)stellar companions shape the winds of evolved stars"*, Science, vol. 369, pp. 1497-1500, (2020).

Eaton D.G. et al., *"GNU Octave version 7.1.0 manual: a high-level interactive language for numerical computations."*, URL https://www.gnu.org/software/octave/doc/v7.1.0/, (2022).

Gaia Collaboration (Brown, A. G. A., et al.), *"Gaia Data Release 2"*, Astronomy & Astrophysics,

vol. 616, pp. A1, (2018).

Herwig F., *"Evolution of Asymptotic Giant Branch Stars"*, Annual Review of Astronomy & Astrophysics, vol. 43, no. 1, pp. 435-479, (2005).

Hirano N. et al., *"High velocity bipolar outflow and disk-like envelope in the carbon star V Hya"*, American Astronomical Society, vol. 616, pp. L43-L46, (2004).

Höfner S. and Olofsson H., *"Mass loss of stars on the asymptotic giant branch"*, Astronomy & Astrophysics Review, vol. 26, no. 1, (2018).

Hogerheijde M. R. and van der Tak F. F. S., *"An accelerated Monte Carlo method to solve two-dimensional radiative transfer and molecular excitation"*, Astronomy & Astrophysics, vol. 362, pp. 697-710, (2000).

Keto E., *"Radiative transfer modeling of radio-frequency spectral line data - Accretion onto G10.6 - 0.4"*, The Astrophysical Journal, vol. 355, p. 190, (1990).

Keto E. and Caselli P., *"The Different Structures of the Two Classes of Starless Cores"*, The Astrophysical Journal, vol. 683, pp. 238-247, (2008).

Keto E. and Rybicki G. B., *"Modeling molecular hyperfine line emission"*, The Astrophysical Journal, vol. 716, no. 2, pp. 1315-1322, (2010).

Kharchenko N. V. and Roeser S., *"VizieR Online Data Catalog: I/280"*, (2009).

Kim H. et al., *"Circumstellar molecular composition of the oxygen-rich AGB star IK Tauri"*, Astronomy & Astrophysics, vol. 516, p. A68, (2010).

Kwok S. et al., *"On the origin of planetary nebulae"*, The Astrophysical Journal, vol. 219, p. L125, (1978).

Kwok S., *"On the Origin of Morphological Structures of Planetary Nebulae"*, Galaxies, vol. 6, no. 3, p. 66, (2018).

LeDrew G., *"The Real Starry Sky"*, Journal of the Royal Astronomical Society of Canada, vol. 95, pp. 32-33, (2001).

Loughnane R. M. et al., *"Modeling Star-Forming Regions using a 3D Molecular Transport Code"*, ASP Conference Proceedings, vol. 453, pp. 33L, (2012).

Mauron N. and Huggins P. J., *"Imaging the circumstellar envelopes of AGB stars"*, Astronomy & Astrophysics, vol. 452, pp. 257-268, (2006).

Neri et al. R., *"A ^{12}CO ($J = 1 \rightarrow 0$) and ($J = 2 \rightarrow 1$) atlas of circumstellar envelopes of AGB and post-AGB stars"*, Astronomy & Astrophysics Supplement Series, vol. 130, no. 1, pp. 1-64, (1998).

Neugebauer G. et al., *"Observations of Extremely Cool Stars"*, Astronomy & Astrophysics, vol. 142, pp. 399-401, (1965).

Olofsson H. et al., *"A study of circumstellar envelopes around bright carbon stars. I - Structure, kinematics, and mass-loss rate."*, The Astrophysical Journal Supplement Series, vol. 87, p. 267, (1993).

Olofsson H. et al., *"Circumstellar molecular radio line intensity ratios"*, Astronomy & Astrophysics, vol. 329, pp. 1059-1074, (1998).

Osterbrock D., *"Planetary Nebulae"*, Annual Review of Astronomy & Astrophysics, vol. 2, no. 1, pp. 95-120, (1964).

Parker Q. et al., *"The Macquarie/AAO/Strasbourg H Planetary Nebula Catalogue: MASH"*, Monthly Notices of the Royal Astronomical Society, vol. 373, no. 1, pp. 79-94, (2006).

Rawlings J. et al., *"HCO^+ emission excess in bipolar outflows"*, Monthly Notices of the Royal Astronomical Society, vol. 351, no. 3, pp. 1054-1062, (2004).

Rybicki G.B. and Hummer D.G., *"An accelerated lambda iteration method for multilevel radiative transfer"*, Astronomy & Astrophysics, vol. 245, pp. 171-181, (1991).

Santander-García M. et al., *"SHAPEMOL: a 3D code for calculating CO line emission in planetary and protoplanetary nebulae"*, Astronomy & Astrophysics, vol. 573, pp. A56, (2015).

Schöier F. L. et al., *"An atomic and molecular database for analysis of submillimetre line observations"*, Astronomy & Astrophysics, vol. 432, pp. 369-379, (2005).

Schröder K. -P. et al., *"Tip-AGB stellar evolution in the presence of a pulsating, dust-induced "superwind""*, Astronomy & Astrophysics, vol. 349, pp. 898-906, (1999).

Soker N., *"Shaping Planetary Nebulae and Related Objects"*, Astronomical Society of the Pacific Conference Series; Astronomical Society of the Pacific: San Francisco, CA, USA,Volume 313, p. 562, (2004).

Steffen W. et al., *"Shape: A 3D Modeling Tool for Astrophysics"*, Astronomy & Astrophysics, vol. 17, pp. 454-465, (2006).

van Zadelhoff G. -J. et al., *"Numerical methods for non-LTE line radiative transfer: Performance and convergence characteristics"*, Astronomy & Astrophysics, vol. 395, pp. 373-384, (2002).

Wheeler J. et al., *"Arp 220: New Observational Insights into the Structure and Kinematics of the Nuclear Molecular Disks and Surrounding Gas"*, The Astrophysical Journal, vol. 896, pp. 43, (2020).

Wong K. T. et al., *"Circumstellar ammonia in oxygen-rich evolved stars"*, Astronomy & Astrophysics, vol. 612, pp. A48, (2018).

Wood P. and Zarro D., *"Helium-shell flashing in low-mass stars and period changes in mira variables"*, The Astrophysical Journal, vol. 247, pp. 247-256, (1981).

Yang B., *"Rotational quenching of CO due to H_2 collisions"*, The Astrophysical Journal, vol. 718, pp. 1062-1069, (2010).